



**HAL**  
open science

## A novel laser-based method to measure the adsorption energy on carbonaceous surfaces

D. Duca, C. Pirim, M. Vojkovic, Y. Carpentier, A. Faccinetto, M. Ziskind, C. Preda, C. Focsa

► **To cite this version:**

D. Duca, C. Pirim, M. Vojkovic, Y. Carpentier, A. Faccinetto, et al.. A novel laser-based method to measure the adsorption energy on carbonaceous surfaces. *Carbon*, 2020, 173, pp.540-556. 10.1016/j.carbon.2020.10.064 . hal-03418708

**HAL Id: hal-03418708**

**<https://hal.science/hal-03418708v1>**

Submitted on 8 Nov 2021

**HAL** is a multi-disciplinary open access archive for the deposit and dissemination of scientific research documents, whether they are published or not. The documents may come from teaching and research institutions in France or abroad, or from public or private research centers.

L'archive ouverte pluridisciplinaire **HAL**, est destinée au dépôt et à la diffusion de documents scientifiques de niveau recherche, publiés ou non, émanant des établissements d'enseignement et de recherche français ou étrangers, des laboratoires publics ou privés.

# A novel laser-based method to measure the adsorption energy on carbonaceous surfaces

D. Duca<sup>a</sup>, C. Pirim<sup>a</sup>, M. Vojkovic<sup>a</sup>, Y. Carpentier<sup>a</sup>, A. Faccinetto<sup>b</sup>, M. Ziskind<sup>a</sup>, C. Preda<sup>c</sup>, C. Focsa<sup>a,\*</sup>

<sup>a</sup>Univ. Lille, CNRS, UMR 8523 – PhLAM – Laboratoire de Physique des Lasers Atomes et Molécules, F-59000 Lille, France

<sup>b</sup>Univ. Lille, CNRS, UMR 8522 – PC2A – Physicochimie des Processus de Combustion et de l’Atmosphère, F-59000 Lille, France

<sup>c</sup>Univ. Lille, CNRS, UMR 8524 – Laboratoire de Mathématiques Paul Painlevé, F-59000 Lille, France

---

## Abstract

The reactivity of carbonaceous surfaces bears a fundamental role in various fields, from atmospheric chemistry and catalysis to graphene and nanoparticles. This reactivity is mainly driven by the surface chemical composition and by the strength of the interaction between the adsorbates and the surface (physi-/chemisorption). While the surface composition of complex natural samples can be well characterized, adsorption energies (ergo, adsorption processes) of the corresponding adsorbate/adsorbent systems are often overlooked. We propose a novel laser-based method for measuring the adsorption energy of chemical species on various carbonaceous surfaces. The proof of concept of this original method has first been demonstrated by deriving adsorption energies of various systems consisting of polycyclic aromatic hydrocarbons and activated carbon. The great potential of this fast, spatially resolved, and surface-sensitive method, which can also act as a defect density probe at the mesoscale, has been further demonstrated through the study of systems of increasing complexity.

*Keywords:* Carbonaceous surfaces, Adsorption energy, Laser-induced thermal desorption, Mass spectrometry, Bayesian statistics

---

## 1. Introduction

Carbonaceous materials are used in a wide range of applications including aerospace and defense, automotive, energy, construction, electronics, and sports. Their superior properties including excellent stiffness, high tensile strength, low thermal expansion, and good temperature tolerance [1, 2], make them versatile materials that can be shaped into various forms depending upon the use intended (*e.g.* carbon fibers, carbon nanotubes, graphene). Carbon-based materials can also be turned into metal-free catalysts and serve as a promising alternative to transform sustainable biomass into renewable energy systems [3].

Due to their excellent adsorption capacities, carbonaceous materials are widely employed as filtration media. Carbon nanotubes (CNT) show great

potential at revolutionizing water and gas treatment technologies [4] as they provide much higher surface areas, adsorption capacities, and faster kinetics than activated carbon, the currently prevailing filtration agent. The utility of the adsorptive fixation of organics in the gas and liquid phases for treating wastewaters and emission gasses is already showcased for a number of harmful compounds [5–8]. Another considerable advantage of carbon nanostructures is that their properties can be tailored to target certain chemical species (*e.g.* toxins, heavy metal ions) [4, 9, 10].

For carbonaceous materials, the downside of exhibiting high adsorptive capacities is that they will act as surface carriers. This can lead to adsorbed toxic species undergoing long-range transport in the atmosphere. This effect is commonly observed with combustion generated aerosols (soot), which consist of a carbonaceous matrix often coated with a plethora of organic species [11–13], many of them exhibiting a proven carcinogenic potential [14–16].

---

\*Corresponding author. Tel.: +33 675 482 049

Email address: cristian.focsa@univ-lille.fr (C. Focsa)

39 This makes the impact of combustion generated  
40 particles on human health considerably greater, es-  
41 pecially since their inhalation can result in health  
42 problems beyond the lungs [17]. In fact, the pres-  
43 ence of combustion derived nanoparticles has been  
44 detected in the frontal cortex of autopsy brain sam-  
45 ples [18], urine of healthy children [19], and even in  
46 the fetal side of the placenta [20]. If transported  
47 to the fetus, these particles – as surface carriers for  
48 potentially toxic species – could significantly affect  
49 fetal health and development [20].

50 In this context, the benefit of identifying the ad-  
51 sorption mechanism on carbonaceous surfaces and  
52 its associated adsorption energy is threefold. It can  
53 provide necessary information to better compre-  
54 hend, and potentially minimize, the health impact  
55 of carbonaceous aerosols. It can help design bet-  
56 ter carbon-based materials for industrial use. And  
57 finally, it can offer some insights into the complex  
58 and still only partially understood soot formation  
59 mechanism since adsorption energies define whether  
60 the surface species (adsorbates) are chemisorbed or  
61 physisorbed, and therefore if the surface molecu-  
62 lar compounds result from surface chemistry (rem-  
63 nants of the soot formation) or physical condensa-  
64 tion [21].

65 Adsorption performances are governed by phys-  
66 ical and chemical parameters that greatly vary  
67 across adsorbate/adsorbent systems. Thus, a sys-  
68 tematic study needs to be undertaken in order to  
69 determine i) to what extent the adsorption energy  
70 depends on the nature and the size of the adsorbate,  
71 and ii) the type of interactions established between  
72 adsorbate and adsorbent. Depending upon the na-  
73 ture of the adsorbate (gas or liquid) and adsor-  
74 bent (polycrystalline film, single-crystal, oxides, or  
75 nanoparticle surfaces, powders suspended in a liq-  
76 uid or loose powders) [22], various microcalorime-  
77 try techniques, such as single-crystal adsorption  
78 calorimetry (SCAC), isothermal titration calorime-  
79 try (ITC), and differential scanning calorimetry  
80 (DSC) [23, 24], or temperature-programmed des-  
81 orption (TPD) [25, 26] are commonly used to ei-  
82 ther measure directly the heat of adsorption (mi-  
83 crocalorimetry) [27–29], or infer the activation en-  
84 ergy for desorption (TPD). However, for systems  
85 exhibiting meso or macro scale (micrometer- or sub-  
86 millimeter sized) inhomogeneities or field-collected  
87 samples exhibiting small quantities of matter and  
88 complex compositions (*i.e.* with a multitude of  
89 co-adsorbed species), the use of these conventional  
90 techniques becomes at best arduous and at worst

91 impossible.

92 We propose here an original solution to over-  
93 come the restrictions encountered with more con-  
94 ventional techniques when determining adsorption  
95 energies. Our method relies on laser-induced ther-  
96 mal desorption (LITD) coupled with ultra-sensitive  
97 mass spectrometry detection. The principle of the  
98 method relies on the following stages: the carbona-  
99 ceous sample surface is very rapidly heated by a  
100 (visible) nanosecond laser pulse. The heating is lo-  
101 cal (scale of the laser beam diameter) and transient  
102 (initial temperature regained on a microsecond time  
103 scale). A fraction of the molecules adsorbed on  
104 the sample surface is therefore desorbed and subse-  
105 quently ionized by a second (UV) laser pulse before  
106 being mass-selectively detected by a time-of-flight  
107 mass spectrometer. Low desorption and ionization  
108 laser fluences are used to prevent fragmentation of  
109 the analytes or alteration of the adsorbent. The  
110 fraction of molecules desorbed from an irradiated  
111 spot depends on the laser fluence and the number  
112 of pulses it is exposed to. These relationships are  
113 specific to each adsorbate/adsorbent system and in-  
114 dicative of the interaction between the two compo-  
115 nents. The resulting experimental data can then be  
116 mathematically treated to derive the corresponding  
117 adsorption energy.

118 We present in this paper two distinct experimen-  
119 tal approaches, derived from the same LITD prin-  
120 ciple, along with two mathematical models (and  
121 associated statistical procedures) we developed to  
122 retrieve the adsorption energy from the recorded  
123 experimental data. The method is validated on  
124 well-controlled laboratory-synthesized samples, as-  
125 sociating several carbonaceous adsorbents and or-  
126 ganic/inorganic adsorbates at sub-monolayer con-  
127 centration, in a broad range of adsorption energies  
128 (0.2 – 1.5 eV).

## 129 2. Materials and Methods

### 130 2.1. Experimental approaches

131 Two distinct approaches based on the LITD prin-  
132 ciple were followed to collect experimental data for  
133 adsorption energy determination: the “signal de-  
134 cay” and the “fluence curve”.

#### 135 2.1.1. Signal decay

136 The principle of this first experimental approach  
137 is presented in Fig.1a-c: a region of the sample

(delimited by the laser spot on the surface) is irradiated with successive nanosecond laser pulses (10 Hz repetition rate) of constant (low) fluence. For each pulse, a fraction of desorbed molecules is ionized by a second nanosecond laser and further detected by a mass spectrometer. Mass spectra are so recorded for successive laser pulses and the signal corresponding to the adsorbate of interest is plotted as a function of the number of applied laser pulses (Fig. 1c). The pseudo-exponential decay observed simply illustrates a gradual “cleaning” of the irradiated spot by the successive desorption pulses. If this decay is “slow” (*i.e.* a high number of laser pulses is needed to “clean” the surface), then one can infer a strong interaction between the adsorbate and the surface. Conversely, a faster decay (in the same irradiation conditions) will be indicative of looser bonding of the adsorbate to the surface.

### 2.1.2. Fluence curve

The second approach relies on the variation of the desorption yield with the laser fluence, as illustrated in Fig. 1d-e. In this approach, multiple spots on the sample surface are irradiated with only one pulse each, but the pulses exhibit different fluences. Each measurement is performed on different spots of the sample, *i.e.* on a pristine surface that was not previously irradiated, to ensure that the initial concentration is always the same. The different fluences will lead to different temperature increase for each spot and, consequently to different desorption yields. Fitting the fluence variation of the desorption yield with the adequate equation (see below) allows retrieving the adsorption energy.

### 2.2. L2MS set-up

The experimental setup used in this work is based on the L2MS technique [11, 30, 31], which combines three key stages: laser desorption (LD), laser ionization (LI), and time-of-flight mass spectrometry (ToF-MS). The sample is mounted onto a copper holder maintained at constant temperature (170 – 190K in this study) by a regulating device consisting of a heating resistor and a liquid nitrogen closed loop. Initially developed for studies on ice samples [32, 33], this system has proved its efficiency in preventing volatile analyte evaporation at the working pressure ( $\sim 10^{-8}$  mbar) of the mass spectrometer on many combustion-related [11, 30, 34, 35] or PAH-containing [31, 36] samples.

The sample surface (placed vertically, Fig. 2) is irradiated at normal incidence by the 4 ns pulsed

beam of an Nd:YAG laser (Continuum Minilite, second harmonic,  $\lambda = 532$  nm). The desorption laser beam hits the surface with a quasi-top-hat profile of  $\sim 0.7$  mm diameter (measured with a Gentec Beamage-4M beam profiler). The quasi top-hat transverse intensity profile is obtained from the laser output beam by first enlarging it with a beam expander built around a set of convergent and divergent lenses, and then selecting the quasi-flat central region ( $\sim 5\%$ ) of the beam with a diaphragm, which is further image relayed onto the sample surface using a convergent lens.

The desorbed neutral molecules form a forward-peaked plume (*i.e.* narrow angular distribution around the revolution symmetry axis) which propagates at high speed [31, 37] from the sample surface toward the ionization zone. Neutral molecules from the desorbed plume are ionized following a two-photon ionization process [30, 38] using another 4 ns pulsed laser beam (Continuum Powerlite,  $\lambda = 266$  nm, 10 Hz repetition rate,  $\sim 1$  mm diameter, top-hat) propagating orthogonally ( $y$  direction, Fig. 2) to the desorption plume axis. The ionization laser beam intercepts the desorption plume in between the extraction electrodes of an 1 m long, reflectron time-of-flight mass spectrometer (RM Jordan, mass resolution  $m/\Delta m \sim 1000$ ) at  $d \sim 3$  cm from the sample surface. The delay between the desorption and ionization pulses is set to 100  $\mu$ s by a digital delay/pulse generator (SRS DG535).

The ions thus generated are extracted and accelerated ( $x$  direction) toward the free-field flight tube of the mass spectrometer. Mass spectra are recorded with a digital oscilloscope (LeCroy Waverunner 6200A) at a time resolution of 2 ns/point. Data acquisition is controlled by a dedicated routine developed in LabView (National Instruments). Experimental data points considered in this work and amenable to mathematical treatment represent integrated peak areas corresponding to a given analyte, which includes all the peaks associated with its isotopic distribution.

### 2.3. Surface evolution upon irradiation

The desorption fluence is carefully adjusted to be in the low, pre-ablation regime [11, 30], which ensures the desorption of neutral species from the surface of the sample without affecting the underlying carbonaceous matrix. Upon irradiation, the sample surface undergoes temperature variations of large magnitude (1500–2000 K) over a

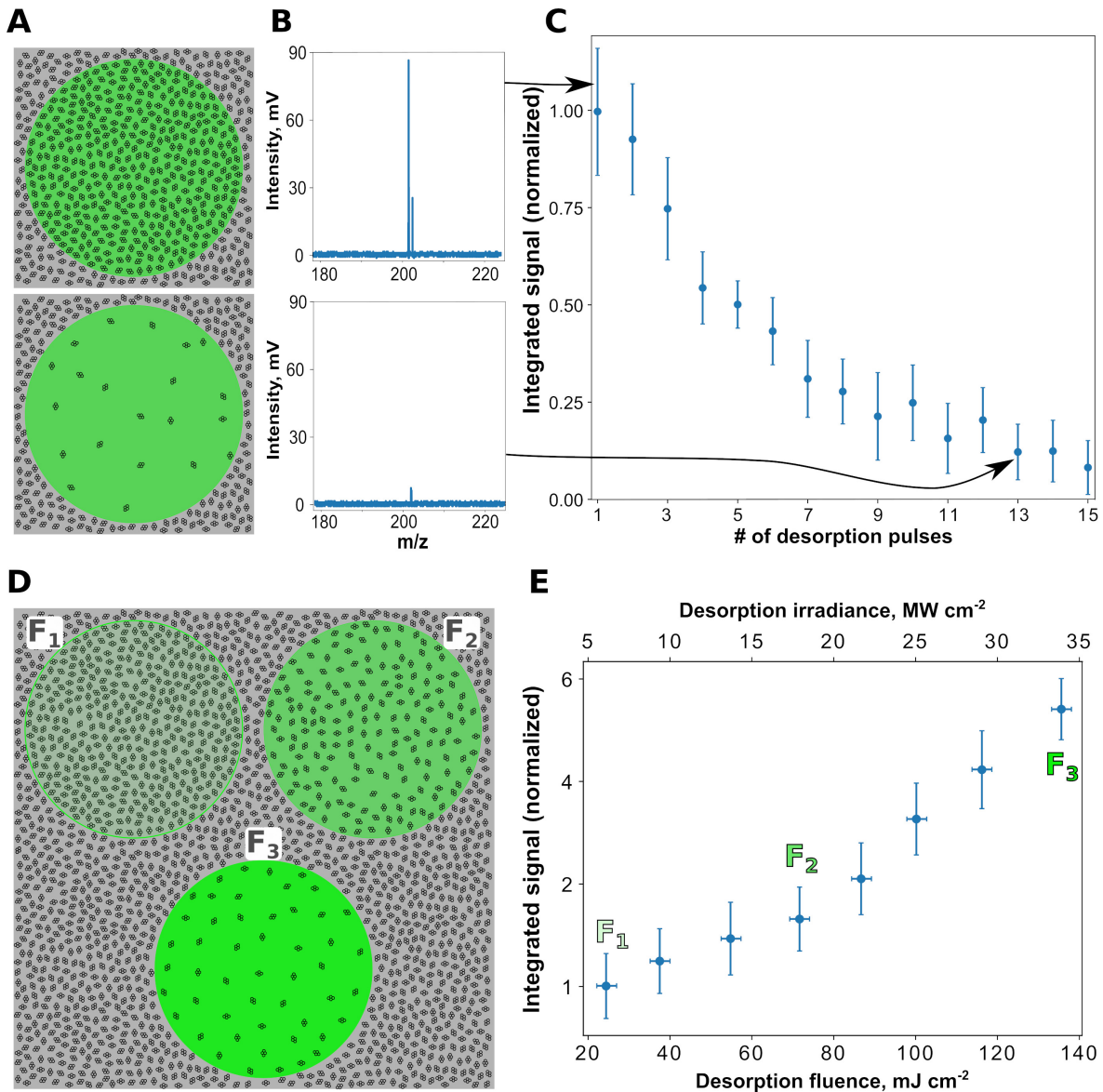


Figure 1: The top and bottom rows describe the “signal decay” and the “fluence curve” experimental approaches, respectively, used to obtain the two distinct datasets from which adsorption energies were subsequently derived. (a) Schematics of the adsorbate coverage evolution upon successive laser pulses of constant fluence applied on the same spot on the sample surface, (b) recorded mass spectra corresponding to two distinct desorption laser pulses (top – 1<sup>st</sup> pulse, bottom – 13<sup>th</sup> pulse), and (c) recorded signal decay. (d) Schematics of the “fluence curve” approach – different spots of the sample irradiated with single laser pulses of various fluences, (e) recorded “fluence curve” signal.

238 very short period of time (the surface typically re- 246  
 239 gains its initial temperature in about 1  $\mu$ s). De- 247  
 240 spite the high temperature reached by the surface 248  
 241 (for only nanoseconds), it was demonstrated that 249  
 242 such a fast-transient process, when generated with 250  
 243 low fluence pulses as performed here, does not 251  
 244 ablate the adsorbent [11]. Moreover, our fluence 252  
 245 optimization procedure shows that mass spectra are 253

devoid of any fragments originating from the ad-  
 sorbate throughout the whole fluence regime used  
 in this work. Therefore, our measurements demon-  
 strate that such fluence regime prevents the frag-  
 mentation of the desorbed molecules and precludes  
 ablation of the adsorbent.

In regards to possible adsorbent nanostructure  
 rearrangement upon fast-transient heating, previ-

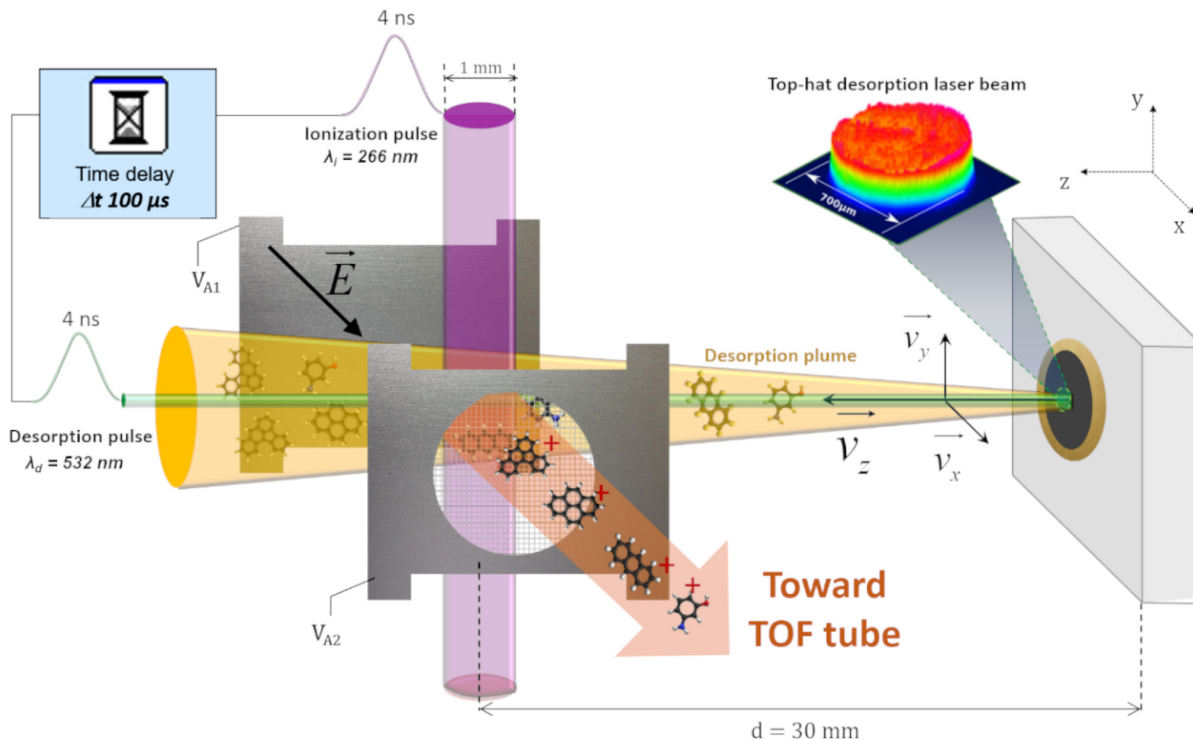


Figure 2: Schematic representation of the laser desorption / laser ionization / ToF-MS experimental arrangement. The desorption laser beam (green) with a top-hat transverse beam profile forms a  $700 \mu\text{m}$  spot on the sample surface. The desorbed neutral molecules form a “plume” (dark yellow) which propagates from the sample surface ( $z$  axis) toward the ionization region situated in between the extraction electrodes of the ToF-MS. A pulsed UV ionization laser beam (purple,  $y$  axis) intersects the desorption plume  $100 \mu\text{s}$  after the desorption beam hits the surface. The obtained ions are then extracted and accelerated ( $x$  axis) toward the field-free flight tube of the ToF-MS.

ous works on amorphous carbon films [39] or black carbon nanoparticles [40] irradiated by nanosecond Nd:YAG laser pulses showed that no significant change in the sample structure was induced in the low fluence regime (typically  $< 50 \text{ mJ cm}^{-2}$ ). In the work of Abrahamson et al. [40], multi-wavelength pyrometry was used to measure transient surface temperatures of more than  $2000^\circ\text{C}$ , while no notable difference in carbon nanostructure was observed by transmission electron microscopy (*i.e.* no rearrangement).

In the first (“signal decay”) experimental approach followed in our work, when a single region of the surface (adsorbent) is irradiated with successive nanosecond laser pulses resulting in the gradual desorption of the adsorbate, it is worth noting that the changing adsorbate surface concentration upon subsequent irradiations does not affect the thermal and optical properties of the system as long as the chemical species are transparent to the desorption

pulse ( $\lambda_d = 532 \text{ nm}$ ) and as the system exhibits a very low surface coverage (both conditions met in this work). As the L2MS technique involves the fast removal of species from the vicinity of the sample [31, 37], re-adsorption of desorbed species is negligible. In addition, any lateral diffusion of molecules across the surface that could potentially replenish the laser spot in between two consecutive desorption laser pulses ( $100 \text{ ms}$ ) can be neglected. For instance, it would take minutes for a pyrene molecule to travel a distance of  $1 \mu\text{m}$  on a carbon surface [41]. Therefore, the physical characteristics of the sample will not change with the increasing number of desorption pulses and thus not influence the desorption process.

#### 2.4. Sample preparation

The development and validation of a method for adsorption energy determination requires well characterized samples. Moreover, the reproducibility of

the method could be assessed only if the characteristics of the sample are held constant. As this work focuses on desorption from carbonaceous surfaces, combustion-generated particles (soot) would have been an appealing candidate as object of study, however, they usually exhibit a very high variability, as their characteristics (*e.g.* specific surface, porosity) depend highly on the combustion conditions. In this context, laboratory-prepared “synthetic soot” [11] represents an interesting alternative as it exhibits a structure akin to that of real soot but has a known and controllable surface chemical composition.

Synthetic soot is prepared here following the protocol described in our previous work [11]. Briefly, polycyclic aromatic hydrocarbons (pyrene and coronene, Sigma Aldrich, 98% purity) are dissolved into dichloromethane (Sigma Aldrich, 99% purity) to make mother (stock) solutions of known concentrations. To these stock solutions are added activated carbon particles (Pureblack 100 Carbon, average particle diameter 80 nm, specific surface area 80–150 m<sup>2</sup>g<sup>-1</sup>) and the resulting mixtures are magnetically stirred for 2 hours. The mixtures are then filtered using a vacuum filtration system employing a quartz fiber filter (Pall Tissuquartz QAT- UP 2500). This filtration step yields, on the one hand, a quartz fiber filter covered by a sub-millimeter thick soot layer infused with the stock solution, and, on the other hand, a filtered solution whose remaining concentration in PAHs can be determined by UV-Vis absorption spectroscopy and subsequent comparison with the stock solution (see Figure S1a). Specifically, as the measured absorbance and the molar concentration are directly proportional in the concentration range studied here, molar concentrations can be estimated knowing the molar extinction coefficient of the solution at a given wavelength and path length. From absorbance measurements of stock solutions of known concentrations can thus be deduced the molar concentrations of the filtered solutions. Therefore, by comparing the absorbance of the stock solution and that of the filtered solution (Figure S1b), it is possible by difference to retrieve the concentration of PAHs remaining on the filter, assuming volatility losses during the preparation steps are negligible [11]. Finally, the surface concentration of PAHs adsorbed on activated carbon particles is calculated knowing the PAH concentration and the specific surface of the particles deposited on the filter.

Three different samples containing either organic

or inorganic species were prepared using the described procedure (Table 1). This included systems containing either a single or two co-adsorbed compounds. Pyrene and coronene were chosen here as adsorbates because of the well-known presence of polycyclic aromatic hydrocarbons (PAH) on the surface of soot particles sampled from real combustors [11, 12]. Additionally, Pb – a heavy metal commonly found in industrial wastewater and usually removed using various carbonaceous materials [9, 10], was used to validate the method for inorganic species. A similar protocol (but a different solvent – ultra-pure deionized water, Purelab Option-Q) was used for the preparation of the lead samples from PbCl<sub>2</sub> salt (Sigma Aldrich, 98%) and Pureblack activated carbon.

Table 1: List of the samples synthesized for adsorption energy measurements. The surface coverage  $\theta$  (in monolayers, ML) was determined from UV-Vis extinction measurements.

Sample	$\theta$ , ML
Pyrene / activated carbon	$2 \cdot 10^{-3}$
(Pyrene + coronene) / activated carbon	$8 \cdot 10^{-3}$ (pyrene) $1.2 \cdot 10^{-2}$ (coronene)
Pyrene / graphite sheet	$\lesssim 10^{-3}$
Pyrene / HOPG	$\lesssim 10^{-3}$
Pb / activated carbon	$\lesssim 10^{-3}$

In order to study the influence of the surface defect density on the retrieved adsorption energy, two more samples based on (mm-thick) graphite sheet and highly oriented pyrolytic graphite (HOPG) adsorbents were prepared in a similar way as the synthetic soot, with the exclusion of the vacuum filtration step. Graphite (Alfa Aesar, graphite sheet) and HOPG (Sigma Aldrich) exhibit significantly lower specific surface areas compared to activated carbon. The resulting adsorbate surface concentration is therefore at the limit of detection of the spectrophotometric method [11]. For this reason, only upper coverage limits ( $\sim 10^{-3}$  ML) are provided in Table 1.

Considering the low coverages and the preparation protocol used in this work, we can assume first that no lateral interaction between adsorbate molecules is present, and second that the coverage is homogeneous across the surface. A low coverage also reduces the possibility of adsorbates forming islands of stacked molecules [42] and thus ensures that the only interaction probed is between adsorbates and the adsorbent surface. Moreover, under these experimental conditions any lateral diffusion

385 of molecules across the surface that could poten- 432  
386 tially replenish the irradiated spot between desorp- 433  
387 tion laser pulses can be neglected [41]. 434

### 388 2.5. Repeatability 435

389 To account for possible experimental fluctuations 436  
390 (mainly due to desorption and ionization lasers), 437  
391 several equivalent measurements are performed in 438  
392 different zones of the same sample. The ana- 439  
393 lyzed regions are chosen not to overlap and there- 440  
394 fore all measurements are considered self-contained. 441  
395 Specifically, for the first experimental approach 442  
396 (signal decay), four signal decays are recorded for 443  
397 the same laser set-point, each decay in a pristine 444  
398 sample zone. For the second experimental approach 445  
399 (*i.e.* fluence curve), four experimental data points 446  
400 per desorption fluence value are acquired on four 447  
401 distinct (pristine) zones of the sample (*e.g.* for 448  
402 pyrene, seven desorption fluence values are utilized 449  
403 which results in 28 experimental datapoints in to- 450  
404 tal). As all measurements are performed in dif- 451  
405 ferent spots on the sample, each datapoint is fully 452  
406 independent. Therefore, different combinations of 453  
407 these points can be made to build distinct “fluence 454  
408 curves”. Among all possible combinations, a to- 455  
409 tal of 10 distinct fluence curves are constructed by 456  
410 randomly combining experimental datapoints. 457

## 411 3. Theory 458

### 412 3.1. Background 459

413 When a pulsed laser beam hits a sample surface, 460  
414 a part of its energy (determined by the physical 461  
415 properties of the irradiated material) is passed on 462  
416 to the sample and induces a temperature jump that 463  
417 may i) trigger the desorption of adsorbates possibly 464  
418 present on the surface, ii) alter the surface (nanos- 465  
419 structure changes), or even iii) ablate micro-volumes 466  
420 of sample. This study is performed in the frame- 467  
421 work of the first effect, known as laser-induced ther- 468  
422 mal desorption (LITD). The pulsed laser-induced 469  
423 heating increases the temperature of surfaces at 470  
424 high rates (up to  $\sim 10^{11}$  K s<sup>-1</sup> with a nanosecond 471  
425 laser [43]), otherwise unattainable with traditional 472  
426 methods (*e.g.* resistive or electron bombardment 473  
427 heating), and is therefore appealing for application 474  
428 to desorption studies. Early studies showed efficient 475  
429 desorption of H, CO, and CO<sub>2</sub> molecules from a 476  
430 variety of surfaces irradiated by pulsed laser beams 477  
431 [44], phenomenon interpreted as a purely thermal 478  
479  
480  
481  
482  
483

effect. This effect was later used to study the ad-  
sorption and desorption kinetics of these species  
by means of relaxation methods [45]. LITD was  
also used to examine the desorption of Na and  
Cs atoms with a sub-monolayer surface concentra-  
tion from Ge (100) substrates [46], of H<sub>2</sub> from Ni  
(100), (110) and (111) [45], of CO from Fe [47] and  
of benzene from Pt (111) surfaces [48]. However,  
none of these studies addressed the determination  
of the adsorption energies from LITD data, as they  
typically used a single high-fluence laser pulse to  
desorb all the adsorbed species from the surface,  
thereby completely “cleaning” the irradiated spot  
of the sample with only one laser pulse. On the  
other hand, when a lower desorption laser fluence  
is used, not all the molecules are desorbed by a  
single laser pulse and multiple, consecutive pulses  
can be applied to the same surface spot [49]. Since  
after each desorption pulse the surface concentra-  
tion of molecules reduces, the amount of desorbed  
compounds decreases after each subsequent laser  
pulse, thus resulting in a pseudo-exponential varia-  
tion of both surface coverage and desorbed amount.  
This variation was first linked to the energetics of  
the adsorbate-adsorbent interaction by Specht and  
Blades [21], who suggested that the decay obtained  
for pyrene desorbing from charcoal corresponds to  
molecules that are weakly bound to the surface,  
while the relatively constant signal that followed  
was associated with molecules having a stronger in-  
teraction with the carbonaceous surface. The ob-  
served decay, however, was not used by the authors  
to derive the strength of the pyrene-surface inter-  
action.

A similar decay was reported by our laboratory  
in a previous work [11] which focused on the cal-  
culation of the detection limit of the two-step laser  
mass spectrometry (L2MS) technique. Although  
the energetics of the analyte-surface bond was not  
studied, we demonstrated at that time that a sin-  
gle form of interaction between the analyte and the  
carbonaceous surface (in this case physisorption)  
can be achieved on surrogate soot samples. A dif-  
ferent approach was proposed by Dreisewerd et al.  
[50] to derive the activation energy of desorption  
from sinapic acid and bovine insulin thick layers  
deposited on stainless steel, based on the evolution  
of the desorbed amount of molecules with the irra-  
diation laser fluence.

The present study builds on this previous works  
and proposes for the first time a complete experi-  
mental, theoretical, and data treatment methodol-



ogy to derive adsorption energies from LITD/L2MS experiments. Moreover, by developing a theoretical model describing LITD, an extra step was taken toward better understanding fast processes occurring at the sample surface.

### 3.2. Desorption of physisorbed species

In the kinetic approach, the desorption is described in terms of the desorption rate – the number of molecules that desorb from a unit of surface per unit of time. Assuming that all adsorbed atoms or molecules occupy identical sites, the desorption rate can be expressed by the Polanyi-Wigner equation [51]:

$$-\frac{d\theta}{dt} = \nu\theta^n \exp\left(-\frac{E_{des}}{k_B T}\right) \quad (1)$$

where  $n$  is the order of the desorption kinetics (usually  $n = 1$  for physisorption),  $E_{des}$  is the activation energy for desorption,  $T$  is the surface temperature, and  $k_B$  the Boltzmann constant. As said above, at the low adsorbate coverages used here ( $10^{-3}$ – $10^{-2}$  monolayers) any interaction between neighbouring adsorbed molecules can be neglected [52], and thus the  $E_{des}$  will be characteristic of the adsorbate-adsorbent interaction only. The first-order pre-exponential factor  $\nu$  (measured in  $\text{s}^{-1}$ ), related with the vibration of the adsorbate-adsorbent bond along the reaction coordinate associated with desorption, is also called attempt frequency and is on the order of the atomic frequency of the crystal lattice ( $\sim 10^{13} \text{ s}^{-1}$ ) [53]. For the atom or molecule to leave the surface it needs to overcome the activation barrier for desorption. Since physisorption is a reversible process, the activation energy of desorption is equal to the adsorption energy:  $E_{ads} = E_{des}$ , and therefore these two terms will be used interchangeably hereafter.

As seen in Eq. (1), the driving force of desorption is the surface temperature. Therefore, to calculate the rate of desorption and subsequently estimate the adsorption energy, one should first determine the temperature variation. A precise calculation of the temperature temporal and spatial variation involves quite a heavy mathematical apparatus. Therefore, some authors [50, 54, 55] have used a simplified LITD description, a steady-state process involving an “effective” temperature that would be reached upon laser irradiation and at which the desorption occurs.

Although a more elaborated, space- and time-resolved model was developed in this study, we also

present here this simplified approach for the sake of comparison with previous works.

### 3.3. “Effective temperature” model

The advantage of this simplified, steady-state approach is that all optical and thermal properties of the sample are expressed by a single factor, thus making it easier to retrieve when fitting experimental data. Moreover, the temperature profile of the sample is not required which significantly reduces the computational time needed by the model. Within this approximation, the number of molecules  $N$  desorbed after a laser pulse can be expressed as [50, 54, 55]:

$$N \approx A \cdot \exp\left(\frac{-E_{ads}}{k_B (T_0 + BF)}\right) \quad (2)$$

where  $A$  is proportional to the surface coverage,  $B$  is a factor that describes the conversion of the deposited energy into the surface temperature increase and is associated (for the low coverage used here) solely with the adsorbant properties,  $T_0$  is the initial temperature,  $F$  the desorption laser fluence at the surface. In this model,  $(T_0 + BF)$  is seen as an “effective” sample temperature which would be reached upon laser irradiation and at which the desorption occurs.

The energy deposited into the sample unit volume is determined by the incident laser fluence, and accounts for the reflectivity  $R$  and the optical absorption coefficient  $\alpha(\lambda_0)$  of the sample at the desorption laser wavelength  $\lambda_0$ . This is expressed through the  $B$  parameter, as follows [50]:

$$B = (1 - R) \frac{\alpha(\lambda_0)}{\rho c} \quad (3)$$

where  $c$  is the specific heat capacity of the sample and  $\rho$  is the sample density. The value of the  $B$  parameter can considerably change depending on the actual sample characteristics; however, a good initial estimation can be obtained with values reported in the literature. Alternatively,  $B$  can be determined by measuring the required physical parameters of the sample prior to the adsorption energy determination. However, this is not always possible in the case of field-collected samples since characterizing micrograms of material can be challenging and adds extra preparation steps that can potentially damage and/or contaminate the sample (often being very expensive to obtain and/or unique). Therefore, the developed model should be

576 able to determine the adsorption energy based on  
 577 only an ‘initial guess’ for the  $B$  parameter. The  $B$   
 578 parameter values calculated for two different adsorbent  
 579 materials used in this work (nano-porous soot and graphite),  
 580 along with the physical constants used in their calculation,  
 581 are presented in Table 2. Note that the  $B$  values presented  
 582 in this table can be only seen as estimates, sufficiently close  
 583 to the real values to be used by the fitting algorithm as  
 584 ‘initial guess’.  
 585

Table 2:  $B$  parameters calculated from Eq. (3) for activated carbon particles and graphite, along with physical parameters sourced from the literature and used in the calculation.

Parameter	Carbonaceous surface	
	Activated carbon particles	Graphite
R	0.2 <sup>a</sup>	0.1 <sup>b</sup>
$\alpha$ , $10^7 m^{-1}$	1.0951 <sup>c,d</sup>	3.4385 <sup>b</sup>
$\rho$ , $10^3 kg m^{-3}$	0.4 <sup>c</sup>	1.9 <sup>d</sup>
$c$ , $J K^{-1} kg^{-1}$	840 <sup>c</sup>	970 <sup>d,e</sup>
B, $J^{-1} K m^2$	26.0	16.2

<sup>a</sup>Ref. [56], <sup>b</sup>Ref. [57], <sup>c</sup>Ref. [11], <sup>d</sup>Ref. [58], <sup>e</sup>Ref. [59]

586 The surface concentration of adsorbed species decreases  
 587 after each desorption pulse, changing the  $A$  factor in Eq. (2).  
 588 The first laser pulse will give  $N_1$  desorbed molecules:  
 589

$$N_1 = p \cdot s \cdot Q_0 \cdot \exp\left(-\frac{E_{ads}}{k_B(T_0 + BF)}\right) \quad (4)$$

590 where  $Q_0$  is the initial adsorbate surface concentration,  
 591  $s$  is the surface area of the irradiated spot, and  $p$  a  
 592 proportionality constant. The number of molecules left on  
 593 the irradiated surface spot will progressively decrease after  
 594 each subsequent laser pulse.  
 595

596 Considering that for the low coverages used here the  
 597 adsorption energy does not change with the surface  
 598 concentration (see Section 2.4) and the physical properties  
 599 of the sample surface do not change upon irradiation with  
 600 successive laser pulses (see Section 2.3),  $N_j$  molecules will  
 601 be desorbed on the  $j^{th}$  desorption pulse:  
 602

$$N_j = p \cdot s \cdot Q_0 \left(1 - p \cdot \exp\left(-\frac{E_{ads}}{k_B(T_0 + BF)}\right)\right)^{j-1} \cdot \exp\left(-\frac{E_{ads}}{k_B(T_0 + BF)}\right) \quad (5)$$

The  $S_j$  signal recorded by the detector will there-

fore be:

$$S_j = m \cdot N_j = m \cdot p \cdot s \cdot Q_0 \left(1 - p \cdot \exp\left(-\frac{E_{ads}}{k_B(T_0 + BF)}\right)\right)^{j-1} \cdot \exp\left(-\frac{E_{ads}}{k_B(T_0 + BF)}\right) \quad (6)$$

603 where  $m$  is a proportionality factor accounting for the  
 604 ionization efficiency, transfer function of the mass spectrometer,  
 605 and detector efficiency.

The variation of the recorded signal can also be expressed  
 607 as a function of the desorption fluence – a “fluence curve”  
 608 that can be obtained with the second experimental approach  
 609 (see Section 2.1.2):

$$S(F) = m \cdot p \cdot s \cdot Q_0 \cdot \exp\left(-\frac{E_{ads}}{k_B(T_0 + BF)}\right) \quad (7)$$

The proposed model can be used to derive the adsorption  
 610 energy of a given analyte from experimental data recorded  
 611 by the mass spectrometer. The adsorption energy of an  
 612 analyte can be retrieved by fitting experimental data either  
 613 with Eq. (6) (signal decay induced by successive laser  
 614 pulses applied on the same surface spot) or Eq. (7) (signal  
 615 variation with fluence). The fitting algorithm requires an  
 616 “initial guess” – a starting point relatively close to the  
 617 actual values. The initial guess for the  $B$  parameter was  
 618 calculated using literature data (Table 2). The initial  
 619 value for the adsorption energy was also sourced from the  
 620 literature (*e.g.* 0.98 eV for pyrene [60, 61]). We note  
 621 however that fitting the signal decay and fluence curves  
 622 with Eq. (6) and (7), respectively, can be challenging as  
 623 they contain two highly correlated parameters. Since the  
 624 “effective” temperature reached by the surface upon laser  
 625 irradiation is significantly higher than its initial  
 626 temperature (*i.e.*  $BF \gg T_0$ ), the adsorption energy  
 627  $E_{ads}$  and the  $B$  parameter are highly correlated. Therefore,  
 628 fitting the proposed model to experimental data requires  
 629 a specific algorithm which is detailed below in Section 3.5  
 630 and Appendices A and B.  
 631  
 632  
 633  
 634

### 3.4. Transient temperature model

#### 3.4.1. Pulsed laser surface heating

The effective temperature desorption model is only a  
 635 crude approximation of the laser-induced thermal  
 636 desorption and to fully model this process the fast  
 637 variation of the sample temperature

641 should be taken into account. A variety of stud-  
 642 ies addressed the fast heating of solid samples ex-  
 643 posed to lasers, describing the processes occurring  
 644 at different wavelengths, laser irradiances, pulse  
 645 lengths and on various target materials [11, 49, 62–  
 646 66]. The approach commonly followed is to de-  
 647 scribe laser–solid interactions at a macroscopic  
 648 scale using the heat conduction equation (although  
 649 some studies treated this phenomenon at an atom-  
 650 istic/molecular level, but on a limited timescale  
 651 [54]). For low-fluence nanosecond laser pulses, the  
 652 energy passed on to the sample does not lead to  
 653 its melting nor its evaporation, therefore no phase  
 654 transition terms are needed in the equations [64].  
 655 Most of the studies focus on the temperature vari-  
 656 ation in the sample volume (*i.e.* along the  $z$  depth  
 657 axis) and not radially on the surface. Moreover,  
 658 the laser pulse is often considered as a surface heat  
 659 source ( $z=0$ ), which does not take into account its  
 660 propagation into the sample volume as described by  
 661 the Beer-Lambert law [11].

662 To calculate sample temperature variations upon  
 663 laser irradiation, the sample was considered as a  
 664 medium characterized by continuous specific heat  
 665 capacity  $c_p$ , thermal conductivity  $k$  and density  $\rho$ .  
 666 Considering a continuum is the approach adopted  
 667 in all previous studies and is justified by the di-  
 668 mension of the probed zone (0.7 mm laser diame-  
 669 ter in our case), which is much larger than possi-  
 670 ble nanoscale heterogeneities, even for nanoporous  
 671 media as the synthetic soot samples studied here.  
 672 Space- and time-resolved temperature profiles were  
 673 calculated with the 3D heat conduction equation:

$$\begin{aligned}
 \rho(T) \cdot c_p(T) \frac{\partial T(x, y, z, t)}{\partial t} = k(T) \left( \frac{\partial^2 T(x, y, z, t)}{\partial x^2} + \right. \\
 \left. + \frac{\partial^2 T(x, y, z, t)}{\partial y^2} + \frac{\partial^2 T(x, y, z, t)}{\partial z^2} \right) + q_H(x, y, z, t)
 \end{aligned} \quad (8)$$

674 where  $T$  is the local sample temperature as a func-  
 675 tion of the time  $t$  and position  $(x, y, z)$ . The term  
 676  $q_H(x, y, z, t)$  describes the heat source which, in this  
 677 case, is the desorption laser pulse. To match the  
 678 characteristics of the laser pulse used in the ex-  
 679 periments, the heat source is represented as a flat  
 680 space profile (equivalent to a top-hat laser profile)  
 681 in the calculations. In the temporal domain, the  
 682 laser beam is represented as a Gaussian pulse. The  
 683 energy of the laser pulse is absorbed by the sample  
 684 according to the Beer-Lambert law, therefore:

$$q_H(x, y, z, t) = \alpha I_0 (1 - R) \cdot f(x, y) \cdot g(t) \cdot e^{-\alpha z}$$

$$f(x, y) = \begin{cases} 1, & \sqrt{x^2 + y^2} \leq r_{des} \\ 0, & \text{otherwise} \end{cases} \quad (9)$$

$$g(t) = \frac{1}{\sigma\sqrt{2\pi}} \cdot \exp\left[-\frac{1}{2}\left(\frac{t-t_0}{\sigma}\right)^2\right], \quad (10)$$

with  $\sigma = \frac{\tau_{des}}{2\sqrt{2\ln 2}}$

685 where  $R$  is the sample surface reflectivity,  $\alpha$  is the  
 686 adsorption coefficient at the desorption wavelength  
 687 (532 nm),  $I_0$  is the pulse peak irradiance. The  
 688  $f(x, y)$  and  $g(t)$  functions define the space and  
 689 time profiles of the pulsed laser beam of radius  $r_{des}$  (top-  
 690 hat) and duration  $\tau_{des}$  (full width at half maximum,  
 691 Gaussian). Previous studies conducted by multi-  
 692 wavelength pyrometry [40] showed no change in the  
 693 structural or optical properties of similar carbona-  
 694 ceous surfaces for a laser-induced transient temper-  
 695 ature increase of more than 2000°C, which is above  
 696 the maximum temperatures reached here. Accord-  
 697 ingly, the  $R$  and  $\alpha$  parameters were kept constant in  
 698 the calculations. The same approach is sometimes  
 699 adopted for simulating the laser-induced incandes-  
 700 cence (LII) of soot nanoparticles, where even higher  
 701 temperatures (4000 K) are reached [67]. Moreover,  
 702 Eqs. (8) and (9) do not include any terms account-  
 703 ing for phase transitions or surface alteration (*e.g.*  
 704 photo/thermal-bleaching) [68] as these do not occur  
 705 at the low desorption fluence values studied here.  
 706 The boundary conditions required to solve Eq. (8)  
 707 are:

$$\begin{cases} T(x \rightarrow \infty, y \rightarrow \infty, z \rightarrow \infty, t) = T_i \\ T(x, y, z, t = 0) = T_i \end{cases} \quad (11)$$

708 where  $T_i$  is the initial temperature of the sample.

The thermal conductivity of nonporous samples  
 (*e.g.* graphite) can be found in the literature [58].  
 For porous materials, such as nano-porous soot  
 (*nps*), the thermal conductivity  $k_{nps}$  strongly de-  
 pends on the porosity as the efficiency of phonon  
 propagation is related to the number of contact  
 points between the nanoparticles forming the sam-  
 ple. In this case, the thermal conductivity  $k_{nps}$  of

the  $nps$  layer can be expressed as [69]:

$$k_{nps}(T) = k_{graph}(T) \left[ (1 - \xi)^{3/2} + \xi^{1/4} \frac{k_{air}(T)}{k_{graph}(T)} \right] \quad (12)$$

where  $k_{graph}$  is the thermal conductivity of bulk graphite [58] and  $k_{air}$  is the conductivity of the air filling the pores. The layer porosity  $\xi$  is given by:

$$\xi = 1 - \frac{\rho_{nps}}{\rho_{graph}} \quad (13)$$

where  $\rho_{nps}$  and  $\rho_{graph}$  are the densities of nano-porous soot and graphite, respectively.

The parameters required to calculate the temperature profile of the studied sample were either taken from the literature [11, 26, 58, 63, 69, 70] or calculated from the values for graphite while accounting for the porosity of the sample (Eqs. (12), (13)). The temperature variations of all parameters required for solving Eq. (8) are presented in Fig. S2 of the Supplementary Material. Physical parameters for the graphite sheet and HOPG samples used in this work are nearly identical which allows us to use the same physical characteristics for these two sets of samples.

Eq. (8) was solved with the COMSOL Multiphysics simulation platform using finite element methods. The temporal and spatial temperature evolutions calculated for nano-porous soot and graphite (Fig. 3) show a fast increase with a maximum value reached at  $t = 5.5$  ns in the center of the irradiated surface, followed by a slower cooling toward the initial sample temperature (on microsecond timescale). The heat-affected sample depth is in the range of  $100 \mu\text{m}$  (Fig. 3b), which is significantly lower than the thickness of the samples used in this study. We note that the obtained depth and temporal profiles follow the same trend as the ones reported by previous similar studies [49, 63, 64], although a direct, quantitative comparison is not possible, as the temperature profiles reported in the literature were computed for different materials and desorption laser characteristics (*e.g.* wavelength, pulse duration, fluence).

### 3.4.2. Time- and space-resolved desorption

Once the temperature profile  $T(x, y, z, t)$  is calculated, a space- and time-resolved desorption mathematical model, including the time-dependence of the desorption rate, the number of molecules desorbed per unit of surface, and the total number of

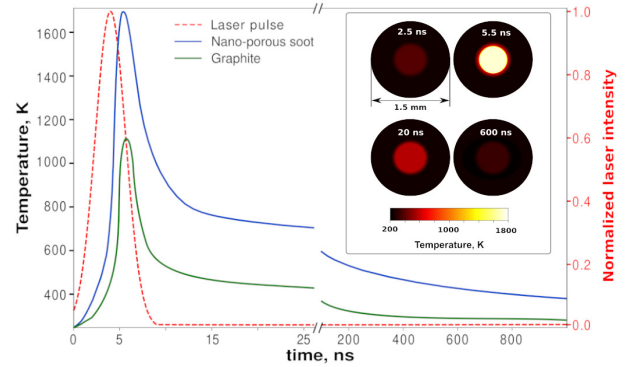


Figure 3: Temporal evolution of the temperature in the center of the irradiated spot ( $T(x = 0, y = 0, z = 0, t)$ ) calculated for nano-porous soot (blue lines) and graphite (green lines) obtained for  $F_{des} = 32 \text{ mJ cm}^{-2}$ . The temporal profile of the desorption laser is plotted for comparison (red dashed line). Snapshots of the radial distribution of the temperature at various delays after the laser pulse are presented in the inset.

molecules desorbed after each desorption pulse can be formulated.

The number of molecules desorbed from the surface after the first laser pulse can be therefore expressed as follows:

$$N_1 = \iint_{-\infty}^{+\infty} Q_0(x, y) \cdot \left( 1 - \exp \left( -\nu \int_0^{\frac{1}{f}} \exp \left( -\frac{E_{ads}}{k_B T(x, y, z = 0, t)} \right) dt \right) \right) dx dy \quad (14)$$

where  $Q_0$  is the initial adsorbate surface concentration and  $f$  is the repetition rate of the desorption laser. The number of molecules desorbed on the  $j^{\text{th}}$  desorption pulse can thus be determined with the following relationship:

$$N_j = \iint_{-\infty}^{+\infty} Q_{j-1}(x, y) \cdot \left( 1 - \exp \left( -\nu \int_0^{\frac{1}{f}} \exp \left( -\frac{E_{ads}}{k_B T(x, y, z = 0, t)} \right) dt \right) \right) dx dy \quad (15)$$

$Q_{j-1}(x, y)$  represents the analyte surface concentration after the  $(j - 1)^{\text{th}}$  desorption pulse (*i.e.* before the  $j^{\text{th}}$  desorption pulse). Since the surface concentration of the analyte decreases after each desorption pulse, the number of desorbing molecules is progressively reduced.

Once a proportionality factor  $m$  is introduced to take into account the overall detection efficiency, the equation can be used for experimental data fitting and adsorption energy retrieval:

$$S_j = m \cdot N_j = m \cdot \iint_{-\infty}^{+\infty} Q_{j-1}(x, y) \cdot \left( 1 - \exp \left( -\nu \cdot \int_0^{\frac{1}{f}} \exp \left( -\frac{E_{ads}}{k_B T(x, y, z=0, t)} \right) dt \right) \right) dx dy \quad (16)$$

where  $S_j$  is the signal recorded by the detector for the  $j^{th}$  desorption pulse. The only unknowns in this equation are the pre-exponential factor  $\nu$ , the adsorption energy  $E_{ads}$ , and the proportionality factor  $m$ . Similarly to the “effective temperature” model, the adsorption energy is determined by fitting the experimental data, in this case with Eq. (16). Compared to the “effective temperature” model, the correlation between the unknown parameters in this equation is much lower which facilitates the fitting procedure. Initial adsorption energy values were sourced from the literature and were the same as in the effective temperature model fits (see above). The initial value for the pre-exponential parameter was taken in accordance with literature recommendations [42, 53, 71] as  $\nu = 10^{12} \text{ s}^{-1}$ .

### 3.5. Data fitting

Fitting the experimental data can be challenging as some of the unknown parameters (*e.g.*  $E_{ads}$  and  $B$  in the “effective temperature” model) are highly correlated. Least-square fitting with functions that contain highly correlated parameters and/or multiple exponential functions can be very unstable, as the outcome of the fit is highly dependent on the initial guess. A *search method* [72] could be used in this case – an algorithm relying on multiple least-square fits of the data performed with different initial values (in user-defined ranges) of the unknown parameters. However, this method is characterized by a rather long convergence time and relatively wide posterior distribution of the retrieved values, and thus was not used here. Instead, we adopted a Markov chains Monte Carlo (MCMC) fitting approach (described in Appendix A) in a Bayesian statistics framework. Starting with initial values for fitted parameters sourced from literature (or calculated based on literature data), several hundred thousands fits are generated to match the experimental data using both the steady-state and transient models. This procedure will return posterior distributions for the fitted parameters. The mode

of these distributions will represent the most probable fit for the given dataset and the confidence intervals will reflect the precision of determination of the unknown parameters from the fit. An illustration is given in Fig.4 for the signal decay of pyrene adsorbed on activated carbon nanoparticles (experimental data averaged over four desorption spots on the same sample,  $2\sigma$  error bars) fitted with the steady-state and the transient temperature models. We notice that both models fit equally well the experimental data, however it is important to emphasize that the red (steady-state model) and green (transient model) dashed lines in Fig. 4a reflect two distinct mathematical concepts. The former results from a severe approximation in that the desorption process occurs at a constant (“effective”) surface temperature, whereas the latter more closely represents the physical reality in that the surface temperature evolves in time and space during the desorption process. The 95% credibility intervals highlighted on the  $E_{ads}$  posterior distributions displayed in Fig. 4b clearly reflect the much lower correlation of the fitted parameters in the transient model with respect to the steady-state one. However, these intervals cannot be used directly to derive “physically-significant” error bars for the adsorption energy, as the developed MCMC fitting algorithm could not converge in a reasonable number of steps (500 000) when large error bars are specified for the experimental data. To derive physically-significant error bars of the fitted parameters, we fitted multiple individual datasets generated from the same sample in the same experimental conditions (see Section 2.5) and further applied an “aggregation of estimators” procedure (see Appendix B) to the fitted parameters values and variances.

## 4. Results

### 4.1. Polycyclic aromatic hydrocarbons on activated carbon nanoparticles

The experimental approaches and the associated mathematical models are first tested using “synthetic soot” samples synthesized in the laboratory (Section 2.4) by (co)adsorbing polycyclic aromatic hydrocarbons on activated carbon nanoparticles at well-controlled, sub-monolayer surface coverages. Pyrene ( $C_{16}H_{10}$ ) and coronene ( $C_{24}H_{12}$ ) were chosen as representative PAHs as they are both known

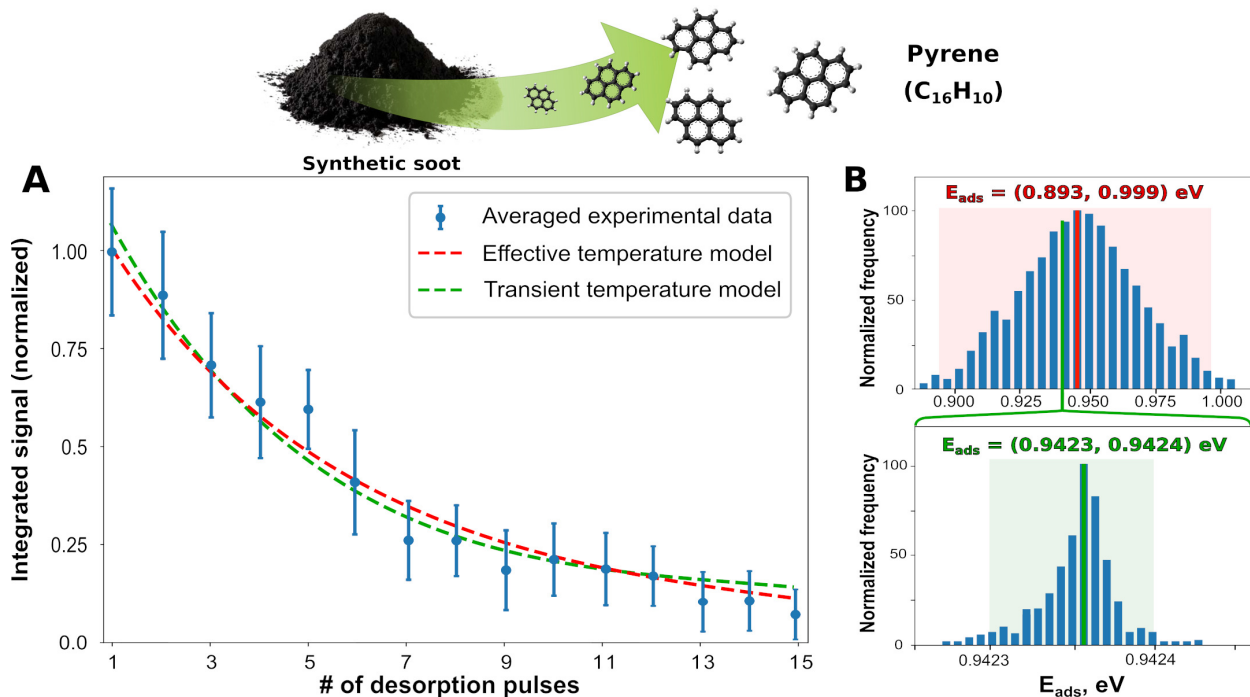


Figure 4: (a) Steady-state (red dashed line) and transient (green dashed line) models fitted to the signal decay curve (four-zone average experimental datapoints) of pyrene desorbing from activated carbon ( $F_{des} = 32 \text{ mJ cm}^{-2}$ ). The plotted fits correspond to the maximum (mode) of the Bayesian posterior distributions shown in (b) – top: steady state, bottom: transient. Shaded areas represent the 95% credibility intervals of  $E_{ads}$ .

853 to be present on combustion generated soot parti- 876  
 854 cles [11–13, 30] and, at the same time, exhibit signifi- 877  
 855 cantly different adsorption energies, which makes 878  
 856 them perfect candidates to test the  $E_{ads}$  recovery 879  
 857 method. Two sets of samples were synthesized, the 880  
 858 first one with a single adsorbed PAH (pyrene), the 881  
 859 second one with both PAHs co-adsorbed on the 882  
 860 same surface. The proposed method allows measur- 883  
 861 ing adsorption energies of co-adsorbed species, 884  
 862 as the signal of multiple mass peaks can be simulta- 885  
 863 neously monitored by time-of-flight mass spectrom- 886  
 864 etry.

#### 865 4.1.1. Pyrene

866 Multiple signal decay and fluence curve datasets 890  
 867 are recorded from the pyrene / activated carbon 891  
 868 surface following the approach described in Sec- 892  
 869 tion 2.5 and the MCMC fitting procedure is ap- 893  
 870 plied to these individual datasets for both steady- 894  
 871 state and transient models. The  $E_{ads}$  initial value 895  
 872 was taken as 0.98 eV from the literature [60] and 896  
 873 this parameter was allowed to vary in the 0.6– 897  
 874 1.2 eV interval for both models. For the steady- 898  
 875 state model, an initial  $B$  value of  $26 \text{ J}^{-1} \text{ K m}^2$  (Ta- 899

ble 2) is used, with an allowed variation interval 15–30  $\text{J}^{-1} \text{ K m}^2$ . In the transient model, a  $10^{12} \text{ s}^{-1}$  initial value is considered for the pre-exponential parameter  $\nu$  in accordance with literature recommendations [53, 71], along with the allowed variation interval  $10^{11}$ – $10^{13} \text{ s}^{-1}$ . Starting with these values, a maximum of 100 000 fits are generated to match the individual datasets with the steady-state and transient models. Both models converge before reaching the maximum number of allowed fits, typically in  $\sim 50\,000$  steps each. The posterior distributions of the  $E_{ads}$ ,  $B$ , and  $\nu$  parameters returned by individual fits are aggregated following the procedure described in Appendix B to calculate the average values and associated error bars ( $1\sigma$ ) listed in Table 3. The obtained data is then used to reconstruct the signal decay and fluence curves, as illustrated in Fig. S3 of the Supplementary Material.

We notice an excellent agreement between the adsorption energies found in both experimental approaches (both signal decay and fluence curve) and by both models. These results are also well in line with the literature value measured for pyrene ad-

900 sorbed on soot particles using thermal desorption 951  
901 kinetics (0.986 eV) [60]. For the “effective temper- 952  
902 ature” model the  $B$  parameters returned by the 953  
903 two approaches ( $B_{decay} = 23.9 \pm 3.4 \text{ J}^{-1} \text{ K m}^2$  and 954  
904  $B_{fluence} = 21.3 \pm 2.1 \text{ J}^{-1} \text{ K m}^2$ ) are in good agree- 955  
905 ment with each other and slightly smaller than 956  
906 the initial estimation ( $26 \text{ J}^{-1} \text{ K m}^2$ ) calculated us- 957  
907 ing literature values. For the transient tempera- 958  
908 ture model, the retrieved pre-exponential factor  $\nu$  959  
909 ( $1.56 \cdot 10^{12} \text{ s}^{-1}$ ) is also close to the initial guess.  
910 Beside validating the analytical method proposed  
911 here, the good agreement with previous works also  
912 confirms that the analyzed samples mimic well soot  
913 samples described in the literature.

#### 914 4.1.2. Pyrene and coronene co-adsorbed

915 Having demonstrated functionality with a single 965  
916 PAH adsorbed onto activated carbon, this adsorp- 966  
917 tion energy calculation method is then put to test 967  
918 using a system consisting of two different polycyclic 968  
919 aromatic compounds co-adsorbed onto the same 969  
920 adsorbant but in such low amount ( $10^{-3} - 10^{-2}$  970  
921 monolayer) that any lateral interactions between 971  
922 them can be neglected. In this configuration, the 972  
923 same laser pulse applied to the surface will lead to 973  
924 the desorption of both molecules, but each with its 974  
925 own kinetics (determined by its adsorption energy 975  
926 value). Signals associated with both molecules are 976  
927 simultaneously recorded by the mass spectrometer 977  
928 to generate individual datasets which are further 978  
929 subjected to the fitting procedure described above, 979  
930 leading to the results displayed in Table 3. 980

931 For the adsorption energy of pyrene, we observe 981  
932 again a very good agreement between the values 982  
933 retrieved by the various experimental / theoretic- 983  
934 al approaches and also with the values determined 984  
935 above, when pyrene was the sole analyte adsorbed 985  
936 onto activated carbon. For coronene, the adsorp- 986  
937 tion energy values determined from various ap- 987  
938 proaches are in excellent agreement with each other 988  
939 and in line with those experimentally determined 989  
940 via temperature programmed desorption measure- 990  
941 ments for coronene adsorbed on carbon nanofibers 991  
942 ( $1.31-1.50 \text{ eV}$ ) [42]. The signal decay and fluence 992  
943 curves of both pyrene and coronene reconstructed 993  
944 from parameters presented in Table 3 overlaid on 994  
945 experimental data are illustrated in Fig. S4 of the 995  
946 Supplementary Material. The  $B$  parameters (char- 996  
947 acteristic of the adsorbent) determined from the 997  
948 two fits of the binary adsorbate / activated carbon 998  
949 sample are in close agreement with each other and 999  
950 also with the ones retrieved for the previous single

adsorbate system (pyrene / activated carbon) shar-  
ing the same adsorbent. Similarly, the  $\nu$  parame-  
ter for pyrene agrees well between the two systems.  
Coronene shows a higher  $\nu$  value (with respect to  
pyrene), as expected from theoretical calculations  
[53, 71]. These results demonstrate the robustness  
of the adsorption energy calculation method from  
LITD experiments and allow us to conceive its ex-  
tension to other adsorbate/adsorbent systems.

#### 960 4.2. Pb on activated carbon nanoparticles

961 Heavy metal ions (*e.g.*  $\text{Pb}^{2+}$ ) are common con- 962  
963 taminants of industrial wastewater and are usu- 964  
965 ally removed using various carbonaceous materials 965  
966 [9, 10]. Thus, the study of the interaction between 966  
967 heavy metals, proven to be carcinogenic even at low 967  
968 concentration, and materials used for their removal 968  
969 from water (*e.g.* activated carbon) is of great im- 969  
970 portance. Detection of lead on soot particles (pre- 970  
971 sumably coming from combustion of leaded gaso- 971  
972 line) was already shown to be possible with laser- 972  
973 based mass spectrometry (*e.g.* Particle Analysis 973  
974 by Laser Mass Spectrometry, PALMS) employing 974  
975 UV ionization of desorbed species [73, 74].  $\text{PbCl}_2$  975  
976 salt was dissolved in deionized water and the re- 976  
977 sulting solution was used to impregnate the acti- 977  
978 vated carbon nanoparticles. Mass spectra recorded 978  
979 upon sample irradiation with the 532 nm laser and 979  
980 ejecta ionization with the 266 nm laser exhibited 980  
981 the characteristic isotopic distribution of  $\text{Pb}^+$  in the 981  
982  $m/z$  204–208 range, presented in Fig. S5 of the Sup- 982  
983 plementary Material. No  $\text{Pb}^{2+}$  signal was present 983  
984 in the mass spectra. Moreover, experiments per- 984  
985 formed with the ionization laser switched off gave 985  
986 no signal in the mass spectra, *i.e.* ionized lead is not 986  
987 directly sampled from the surface. This may seem 987  
988 surprising, as  $\text{Pb}^{2+}$  ions may be formed in the aque- 988  
989 ous solution and be further transferred onto the ad- 989  
990 sorbent surface. Our explanation for this is twofold.  
991 First, the desorption fluence employed (limited by  
992 the carbonaceous surface ablation threshold) might  
993 be too low for desorbing these ions from the sur-  
994 face. Second, the formation of  $\text{Pb}^{2+}$  in the aqueous  
995 solution is only one of many other possibilities, as  
996  $\text{Pb-Cl}$  is not a “pure” ionic bond ( $\Delta\chi_{\text{Pb-Cl}} < 1.7$ ).  
997 Furthermore, in aqueous solution the formation of  
998 an array of (partially) solvated ions is to be ex-  
999 pected. All these ions can then adsorb onto acti-  
vated carbon via different mechanisms (adsorption,  
surface precipitation, ion exchange, sorption, etc.)  
[10, 75–79], and participate to further acid/base,

Table 3: Main parameters derived with the “effective” and transient temperature models. Mean values and error bars are computed using the procedure described in Appendix B. The small number of experimental points for the fluence curve of the pyrene/HOPG system prevented a reliable derivation of the adsorption energy from its fluence curve.

Absorbate	Sample	“Effective temp.” model				Transient temp. model	
		Signal decay		Fluence curve		Signal decay	
		$E_{ads}, \text{eV}$	$B, \text{J}^{-1} \text{K m}^2$	$E_{ads}, \text{eV}$	$B, \text{J}^{-1} \text{K m}^2$	$E_{ads}, \text{eV}$	$\nu, 10^{12} \text{s}^{-1}$
Pyrene	Pyrene / activated carbon	$0.949 \pm 0.049$	$23.9 \pm 3.4$	$0.968 \pm 0.041$	$21.3 \pm 2.1$	$0.965 \pm 0.014$	$1.56 \pm 0.21$
	(Pyrene + coronene) / activated carbon	$0.961 \pm 0.054$	$20.4 \pm 2.8$	$0.983 \pm 0.038$	$22.4 \pm 2.5$	$0.958 \pm 0.018$	$1.31 \pm 0.34$
	Pyrene / graphite sheet	$0.681 \pm 0.019$	$14.1 \pm 1.9$	$0.662 \pm 0.015$	$15.1 \pm 1.4$	$0.696 \pm 0.010$	$1.24 \pm 0.18$
	Pyrene / HOPG	$0.476 \pm 0.021$	$13.5 \pm 1.9$	–	–	$0.508 \pm 0.011$	$1.38 \pm 0.13$
Coronene	(Pyrene + coronene) / activated carbon	$1.519 \pm 0.022$	$22.8 \pm 2.4$	$1.508 \pm 0.024$	$23.1 \pm 1.1$	$1.513 \pm 0.013$	$2.46 \pm 0.15$
Pb	Pb / activated carbon	$0.226 \pm 0.024$	$20.6 \pm 2.3$	$0.206 \pm 0.015$	$21.1 \pm 2.1$	$0.243 \pm 0.011$	$7.46 \pm 0.26$

redox or coordination reactions on the particle surface. A thorough investigation of such a complex surface chemistry is well beyond the scope of the present work.

Both experimental approaches (signal decay and fluence curve) were applied to study the desorption of lead from activated carbon particles. For the signal decay approach, the recorded signal vanishes in fewer desorption pulses compared to aromatic species adsorbed on the same adsorbent (Fig. S6, Supplementary Material). Fitting both models to the experimental data resulted in values for the adsorption energy ( $E_{ads}^{steady} = 0.226 \text{ eV}$  and  $E_{ads}^{transient} = 0.243 \text{ eV}$ , Table 3) close to that found in the literature (0.21 eV for Pb(II) adsorbed on carbon particles obtained from bio waste) [10]. A similar value ( $E_{ads}^{fluence} = 0.206 \text{ eV}$ ) was also determined from the fluence curve (Fig. S6, Table 3). The adsorption energy of lead to carbonaceous surfaces is therefore much lower compared to that of aromatic species [10]. The  $B$  parameter (which is only related to the adsorbent material) is in good agreement (within the limits of the error bars) with the values returned by the steady-state fits on the other samples involving activated carbon (see Table 3). The pre-exponential factor determined from the transient model fit ( $\nu = 7.5 \cdot 10^{12} \text{ s}^{-1}$ ) is in line with theoretical values calculated for small adsorbates [53]. To the best of our knowledge, no  $\nu$  experimental value for this system is reported in the literature.

#### 4.3. Toward the systematic exploration of adsorption energies as a function of adsorbent properties

In order to expand the adsorption energy calculation method to systems of much greater chemical or structural complexity, it is first necessary to explore various adsorbate/adsorbent systems ex-

hibiting significantly different adsorption energies. This can be realized by testing either distinct adsorbates on the same adsorbent or, conversely, the same adsorbate on distinct adsorbents, the latter being studied here. The adsorption energy retrieved corresponds to the average energy of all desorbed molecules. If the irradiated surface contains different types of adsorption sites, each one characterized by a different adsorption energy, then the measured  $E_{ads}$  can be expressed as a weighted average of all possible energy values (*i.e.* energies that correspond to all existing sites). The change in the proportion of adsorption sites of a given type will modify the average and hence the measured (desorption spot averaged) adsorption energy.

Various surface defects can act as adsorption sites (*e.g.* vacancies, impurities) and most of them are present and abundant on the surface of synthetic (and real) soot particles. The adsorption energy of aromatic compounds on adsorbents exhibiting defect-rich surfaces is higher than that expected when the same compounds are adsorbed on a defect-free carbon lattice [80–83]. Accordingly, as the surfaces of materials such as graphite and HOPG contain a much smaller density of defects compared to activated carbon, the adsorption energy of *e.g.* pyrene, on such adsorbents is expected to be substantially lower.

As predicted, the shape of the signal decay curve and the adsorption energy of pyrene desorbed from a graphite sheet and HOPG are noticeably different (Fig. 5). Since the adsorption energy is lower, a smaller number of laser pulses are required to desorb all molecules present on the irradiated spot, hence a shorter signal decay curve is observed. The adsorption energies obtained from the fits performed with the two models (steady-state and transient) are, once again, very similar. Adsorption en-



1076 ergies obtained for pyrene adsorbed on HOPG (Ta- 1128  
 1077 ble 3) are in line with values resulting from ab initio 1129  
 1078 calculations (0.42 – 0.5 eV) [80, 81]. To the best of  
 1079 our knowledge, no experimental measurement for 1130  
 1080 either system (pyrene/HOPG or pyrene/graphite 1131  
 1081 sheet) is reported in the literature. When the adsor- 1132  
 1082 bent is graphite sheet, the adsorption energy value 1133  
 1083 obtained for pyrene ranges between the ones re- 1134  
 1084 trieved for activated carbon and HOPG, which is 1135  
 1085 expected since the surface contains an intermedi- 1136  
 1086 ate number of defects compared to HOPG (fewer 1137  
 1087 defects) and activated carbon (more defects). It is 1138  
 1088 also possible to obtain “fluence curves” for pyrene 1139  
 1089 desorbing from graphite and retrieve the adsorption 1140  
 1090 energy and  $B$  parameter from this approach (Table 1141  
 1091 3). The values for  $E_{ads}$  and  $B$  (0.681 eV and 14.1 1142  
 1092  $J^{-1} K m^2$ , respectively) are also in line with the val- 1143  
 1093 ues obtained from the signal decay. Moreover, the 1144  
 1094 obtained  $B$  values are close to that calculated with 1145  
 1095 literature parameters (16.2  $J^{-1} K m^2$ , Table 2). 1146

1096 Across the various adsorbate-adsorbent systems 1147  
 1097 investigated here (Table 3), the values obtained and 1148  
 1098 trends followed for  $B$  and the pre-exponential  $\nu$  pa- 1149  
 1099 rameters are in accordance with what should be 1150  
 1100 expected in regards of their relationship with ei- 1151  
 1101 ther the adsorbate or the adsorbent. Specifically, 1152  
 1102 as the  $B$  parameter is associated with adsorbent 1153  
 1103 properties (for low adsorbate coverages as studied 1154  
 1104 here), its retrieved value should be comparable for 1155  
 1105 all systems featuring the same adsorbent. This is 1156  
 1106 indeed what is observed in Table 3, since a similar  $B$  1157  
 1107 value was obtained with two different experimental 1158  
 1108 approaches for all cases where desorption from the 1159  
 1109 same adsorbent is studied (*e.g.* 20.4 – 23.9  $J^{-1} K m^2$  1160  
 1110 for activated carbon, Table 3). In contrast, as the 1161  
 1111 pre-exponential factor  $\nu$  is related to the vibration 1162  
 1112 of the adsorbate-adsorbent bond along the reaction 1163  
 1113 coordinate associated with desorption [53], its value 1164  
 1114 should be largely affected by the adsorbate proper- 1165  
 1115 ties. In accordance, Table 3 shows that the value 1166  
 1116 of this parameter significantly varies for systems 1167  
 1117 based on the same adsorbent but different adsor- 1168  
 1118 bates (*e.g.*  $1.56 \cdot 10^{12} s^{-1}$  for pyrene adsorbed on ac- 1169  
 1119 tivated carbon and  $7.46 \cdot 10^{12} s^{-1}$  for lead adsorbed 1170  
 1120 on activated carbon). Such variation with distinct 1171  
 1121 adsorbates was previously reported [42, 53]. Table 1172  
 1122 3 also confirms that the pre-exponential factor  $\nu$  1173  
 1123 values obtained for desorption events involving the 1174  
 1124 same adsorbate are similar (1.24 –  $1.56 \cdot 10^{12} s^{-1}$  1175  
 1125 for pyrene). Finally, beside the consistent evolu- 1176  
 1126 tion of the retrieved  $\nu$  values across the systems 1177  
 1127 studied here, they are also in good agreement with

pre-exponential factors previously reported in the literature.

## 5. Discussion

While it is possible using microcalorimetry to di-  
 rectly appraise the heat of adsorption of a sorbate  
 on various surfaces with a limit of detection (fem-  
 tomole) akin to ours, performing measurements on  
 such distinct samples (loose powder to highly ori-  
 ented surfaces) using a single calorimetric technique  
 can be challenging. A direct comparison with mi-  
 crocalorimetry may be impeded by the fact that we  
 do not study adsorption events taking place from a  
 liquid solution nor directly measure the heat of ad-  
 sorption of a dose of gaseous molecules onto a pow-  
 der or a surface, but instead monitor the desorption  
 of ‘dry’ adsorbates. Temperature-programmed des-  
 orption (TPD) measurements can provide reliable  
 estimates for adsorption energies in experimental  
 conditions close to ours (PAHs already adsorbed  
 on the surface, high vacuum pressure conditions).  
 This technique is thus better suited for comparison  
 purposes. The adsorption energies retrieved using  
 our method are in good agreement with the values  
 reported in the literature from TPD measurements  
 or ab initio calculations. To the best of our knowl-  
 edge, no adsorption energy values determined via  
 (micro/nano)calorimetry techniques are reported in  
 the literature for the adsorbate/adsorbent systems  
 investigated in this work.

The unique features of the new laser-based  
 method proposed here offer some distinct advan-  
 tages with respect to the more conventional tech-  
 niques cited above. First, this method can be  
 applied to systems exhibiting micrometer or sub-  
 millimeter heterogeneities. Specifically, it can be  
 utilized to recover the mean adsorption energy of  
 analytes present in distinct areas of a sample as the  
 lateral resolution is defined by the diameter of the  
 laser spot. The smaller the beam diameter, the bet-  
 ter the lateral resolution. Second, our method re-  
 quires no sample preparation prior to analysis (*e.g.*  
 extraction of material) and necessitates only mi-  
 crograms of materials to operate. It is hence di-  
 rectly applicable to pristine field-collected and nat-  
 ural samples, for which collecting as much as micro-  
 grams of material can be challenging (*e.g.* sampling  
 of aircraft engine [34] or on-road vehicle internal  
 combustion engine emissions [12]). This is partic-  
 ularly important when the focus is on size-selected  
 particles [84, 85] as small as 10 nm, for which the

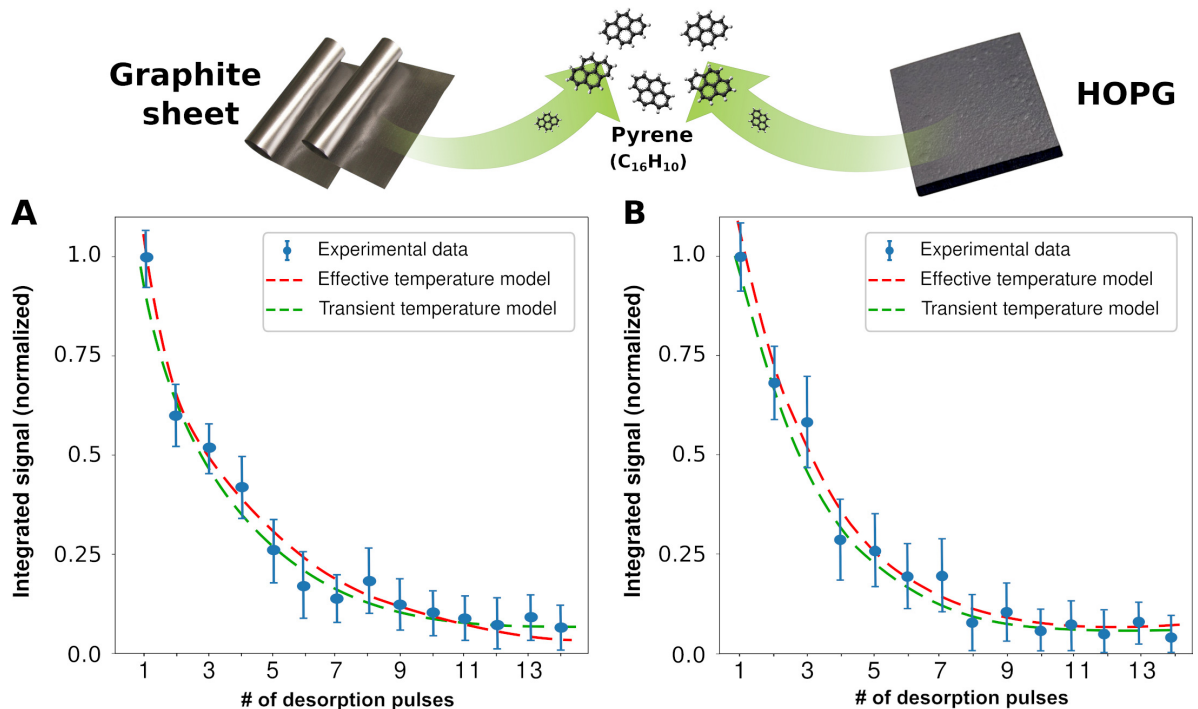


Figure 5: Experimental datapoints (four-zone average) recorded with the “signal decay” approach for pyrene desorbing from (a) graphite sheet ( $F_{des} = 50 \text{ mJ cm}^{-2}$ ) and (b) HOPG ( $F_{des} = 61 \text{ mJ cm}^{-2}$ ). Steady-state (red dashed line) and transient (green dashed line) decay curves calculated with parameters from Table 3.

1178 particle mass lies within the range of attograms. 1202  
 1179 Third, it allows the simultaneous study of one or 1203  
 1180 several analytes coadsorbed on the same surface, 1204  
 1181 which is particularly adapted to real-world complex 1205  
 1182 mixtures. Finally, these particular characteristics, 1206  
 1183 in conjunction with the very low limit of detection 1207  
 1184 (sub-femtomole) that our method provides, consti- 1208  
 1185 tute a valuable solution when more conventional 1209  
 1186 techniques cannot be utilized. 1210

1187 The method we present is sensitive enough to 1211  
 1188 show how the structure of the adsorbent (*e.g.* num- 1212  
 1189 ber of defects) can significantly change the mean 1213  
 1190 adsorption energy. As expected, the adsorption en- 1214  
 1191 ergies derived from our experiments increase with 1215  
 1192 the number of surface defects. This method could 1216  
 1193 act as a surface defect probe and monitor defect 1217  
 1194 densities of various adsorbate/adsorbent systems by 1218  
 1195 following a dedicated and systematic experimen- 1219  
 1196 tal procedure. Different adsorption energies aver- 1220  
 1197 aged over defined zones of a sample surface or 1221  
 1198 between distinct samples can further be related to 1222  
 1199 the disorder/heterogeneity characteristics using, for in- 1223  
 1200 stance, micro-Raman mapping, where deconvoluted 1224  
 1201 Raman maps can be superimposed on adsorption 1225

energy maps of the sample surface probed with the 1202  
 laser. While currently limited to sub-millimeter 1203  
 scale heterogeneities, the lateral resolution could 1204  
 be improved by reducing the diameter of the des- 1205  
 orption laser spot size. The high sensitivity of the 1206  
 technique (ensured by the mass spectrometric de- 1207  
 tection) can be used to finely map spatial variations 1208  
 of physi/chemisorption interactions across hetero- 1209  
 geneous samples, possibly containing small surface 1210  
 inclusions (regions with a distinct composition). 1211

The capabilities of the proposed novel method 1212  
 open perspectives of application in various fields. 1213  
 First, it can serve as a benchmark for adsor- 1214  
 bate/adsorbent systems against which other meth- 1215  
 ods (*e.g.* ab initio calculations) can be compared. 1216  
 On a technological level, it can also encourage the 1217  
 development of advanced materials specially de- 1218  
 signed to selectively target and capture dangerous 1219  
 compounds such as toxins or heavy metal ions [86]. 1220  
 Beyond the obvious interest for catalytic or en- 1221  
 ergy storage materials [87], this method can also 1222  
 be used to characterize thin films grown by phys- 1223  
 ical (pulsed laser deposition, magnetron sputter- 1224  
 ing) [88] or chemical vapor deposition [89] pro-

cesses, which can (depending on the deposition geometry, substrate etc.) exhibit quite large heterogeneities [90, 91] in their adhesion/adsorption properties. The local character of our technique (defined by the laser beam diameter) in conjunction with a fast mathematical treatment (as the simplified effective temperature model) can help in implementing a real-time, spatially-resolved probe directly in the technological process line. Finally, in the combustion field, our method can help shed light on the formation process of soot particles [92, 93] by identifying the origin of the aromatic species present on the surface (i.e. remnants of the nucleation/growth process or condensation from the gas phase).

## 6. Conclusions

Employing laser-induced thermal desorption in conjunction with an adequate mathematical framework, we successfully determine the adsorption energy of distinct adsorbates deposited onto various carbonaceous surfaces. We first formulate and then apply two different mathematical equations modeling the desorption phenomena observed experimentally. The first model describes the desorption process as a steady state phenomenon, using an “effective” sample temperature. This model, while greatly simplifying the calculations, also only constitutes a rough approximation of the desorption process. Advantageous when computational speed is required, it can be used in conjunction with real-time chemical mapping to better characterize the zone of interest. The second model accounts for the fast variation of surface temperature triggered by the absorption of the laser pulse energy. This transient temperature model is more complex but mathematically describes a scenario much closer to physical reality, and also benefits from very little correlation between the variables. Both models fit our experimental data well and provide results close to the values reported in the literature. The adsorption energy is determined for two organic molecules (pyrene and coronene) as well as for an inorganic adsorbate (lead). This approach is also able to retrieve the energy of different compounds co-adsorbed on the same sample (from the same measurements). This serves as a good “proof of concept” for the method, demonstrating that laser-induced desorption combined with our mathematical formulations can be used to study adsorption mechanisms. The novelty and the advantages of

the proposed technique over more traditional approaches in some specific cases along with several new perspectives opened by the developed method were discussed.

Supplementary figures Fig. S1 – S6 can be found in the Supplementary Material at [URL will be inserted by publisher].

## Acknowledgments

This work was supported by the French National Research Agency (ANR) under contract ANR-18-CE22-0019 (UNREAL) and through the PIA (Programme d’Investissement d’Avenir) under contracts ANR-10-LABX-005 (LABEX CaPPA - Chemical and Physical Properties of the Atmosphere) and ANR-11-LABX-0007-01 (Labex CEMPI - Centre Européen pour les Mathématiques, la Physique et leurs Interactions). The authors acknowledge Prof. B Capoen for providing access to the UV-Vis spectrophotometer at Centre d’Etudes et de Recherches Lasers et Applications (CERLA) platform at the University of Lille.

Author contribution: DD, CF, AF, MZ conceptualized the experimental and theoretical method. DD, MV, YC executed the experiments, DD, CPirim, YC, CF discussed the results, DD, CPirim, CF wrote the initial version of the manuscript, DD, CPirim, CF, CPreda developed and validated the mathematical model and the statistical approach. All authors revised and approved the manuscript.

## Appendix A. Markov chains Monte Carlo data fitting

Fitting experimental data with models involving highly correlated parameters requires the use of Bayesian statistics [94–96], which provide powerful tools for estimating complex models where the maximum likelihood-based estimation methods fail. In this framework, several approaches can be followed. Initial tries with the “conventional” *search method* [72] resulted in rather long convergence times and wide posterior distributions of the retrieved parameters (e.g.  $E_{ads}$ ,  $B$ ). In this context, we adopted a Markov chains Monte Carlo (MCMC) approach which converges at a much faster pace.

The MCMC method is designed to estimate the joint posterior distribution of a parameter of interest by random sampling in the probability

1321 space. Many problems described by models containing a large number of free parameters, making them expensive to compute with regular methods (e.g. problems in cosmology and astrophysics that deal with low signal-to-noise measurements [94–96]), have benefited from MCMC. One of the most important benefits of Bayesian data analysis is the ability to minimize the impact of nuisance parameters [96] – parameters that are required to model the studied process but otherwise are not the main objective of the fit. Most uses of the MCMC are based on the Metropolis-Hastings (M-H) method [94–96] or its derivatives and consist of three main parts:

- 1335 • Monte Carlo simulations generating random steps to model complex systems.
- 1336
- 1337 • Markov chains - sequences of events that are probabilistically related to one another. Each event originates from a set of outcomes and each outcome determines the next one, in accordance with a fixed set of probabilities.
- 1338
- 1339
- 1340
- 1341
- 1342 • The acceptance-rejection sampling – an iterative algorithm that generates parameter values from their unknown theoretical posterior distribution.
- 1343
- 1344
- 1345

1346 MCMC allows to generate a data subset covering many possible outcomes of a given system in order to obtain an estimate of the theoretical posterior distribution that can be used to extract statistical measures as mean, median or standard deviation. The simulation process is based on a Markov behavior of the iterative algorithm [95, 96]. An example of a model that can benefit from the use of the MCMC algorithm is the laser-induced thermal desorption, e.g. Eq. 6 of the “effective temperature” model that contains a product of two exponential functions and two highly correlated parameters ( $E_{ads}$  and  $B$ ). The performance of the M-H sampler can be very sensitive to the initial choice of parameters. The result of the MCMC fit will be more reliable for longer chains. For this reason, the first values of the Markov chain are usually dropped. Thus, to determine optimal parameters in a data-driven way, a lengthy “burn-in” period must be used. The burn-in allows to start the MCMC procedure with parameters chosen for convenience that might be located in low probability regions, Fig. A.1a. Once the chain has entered the high-probability region, its states become more representative of the correct distribution (the convergence is achieved). All

1371 the values after the convergence are then used to retrieve the distributions and mode values of all parameters, Fig. A.1b.

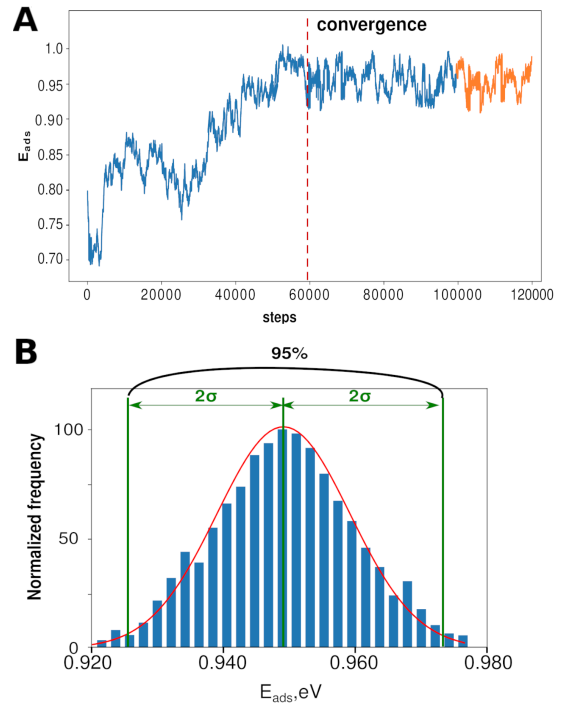


Figure A.1: (a) Example of a Markov chain obtained during fitting of experimental data. The convergence of the fit is depicted with a red dashed line. The last portion of the chain (orange line) is used to determine the posterior distribution of the fitted parameter (b). The distribution is then used to identify the most probable value and the variance of the determined parameter.

## Appendix B. Average value and error bar calculation by estimator aggregation

Individual fits performed on multiple independent datasets generated as described in Section 2.5 return estimated values and associated variances for all parameters of interest through the posterior distributions. As an example, Fig. B.1 illustrates the individual fits of four signal decays recorded in the same experimental conditions (the solid lines represent the “most probable fit” (mode) of the Bayesian posterior distribution for each dataset). In order to account for the measurement variability and determine “physically-significant” average values and error bars associated with the fitted parameters (called “estimators” henceforth), the “inter-

1390 nal” (*i.e.* inside one individual dataset) and “external” 1410  
 1391 (*i.e.* between different datasets, such as A, B, 1411  
 1392 C, D zones in the signal decay approach, Fig. B.1) 1412  
 1393 variances must be combined in an “estimator ag- 1413  
 1394 gregation” methodology [97, 98]. 1414

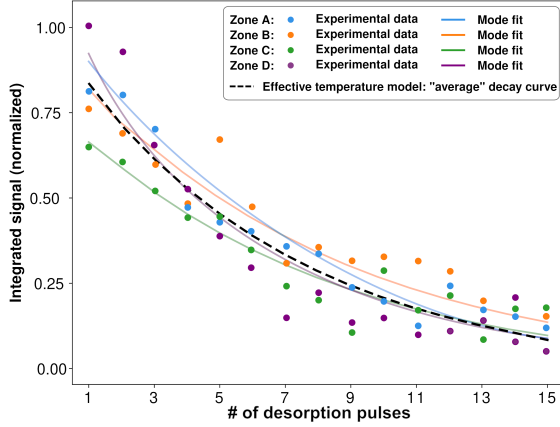


Figure B.1: Symbols: pyrene molecule signal recorded in the same experimental conditions ( $F_{des} = 32 \text{ mJ cm}^{-2}$ ) from four different zones (A, B, C, D) of the same pyrene / activated carbon sample (homogeneous coverage). Solid lines: most probable (mode) fits returned by the Bayesian posterior distribution for each individual dataset. Dashed line: effective temperature model decay curve generated with average parameter values (Table 3).

1395 For a given parameter  $\hat{\beta}$ , let  $\hat{\beta}_i$  be the estimators 1429  
 1396 obtained from data collected in the zone  $i$ , 1430  
 1397  $i \in A, B, C, D$ . Then, the best linear-combination 1431  
 1398 estimator for the  $\hat{\beta}$  parameter with respect to the 1432  
 1399 mean squared error will be: 1433

$$\hat{\beta} = \sum_{i=1}^n \omega_i \hat{\beta}_i \quad (\text{B.1})$$

1400 where  $\omega_i = \frac{\text{Var}^{-1}(\hat{\beta}_i)}{\sum_j \text{Var}^{-1}(\hat{\beta}_j)}$  is the weight associated 1434  
 1401 with each estimator, retrieved from fitting individ- 1435  
 1402 ual datasets (either signal decays or fluence curves). 1436  
 1403 Considering the independence of data recorded in 1437  
 1404 different zones of the sample, the standard deviation 1438  
 1405 of the  $\hat{\beta}$  parameter is given by: 1439

$$\sigma(\hat{\beta}) = \sqrt{\text{Var}(\hat{\beta})} = \sqrt{\sum_i \omega_i^2 (\text{Var}(\hat{\beta}_i) + (\hat{\beta}_i - \hat{\beta})^2)} \quad (\text{B.2})$$

1406 The first term in Eq. (B.2) represents the “internal” 1464  
 1407 variance of each dataset, while the second term 1465  
 1408 represents the “external” variance (*i.e.* between 1466  
 1409 datasets). 1467

The average values and error bars were calculated for the parameters of interest with the described method and reported in Table 3 in the form  $\hat{\beta} \pm \sigma(\hat{\beta})$ . The validity of the method can be verified with the “average” fitting curve (*i.e.* average for all datasets) calculated with the average values for the required parameters. An example of such a curve obtained with the “effective temperature” model is presented in Fig. B.1 (dashed line).

## 1419 References

- 1420 [1] T. D. Burchell, Carbon Materials for Advanced Technologies, Elsevier Science, Oxford, 1999. doi:10.1016/B978-008042683-9/50002-9.
- 1421 [2] A. Jorio, G. Dresselhaus, M. S. Dresselhaus, Carbon Nanotubes. Advanced Topics in the Synthesis, Structure, Properties and Applications, Springer Verlag, Berlin, Heidelberg, 2007. doi:10.1071/978-3-540-72865-8.
- 1422 [3] Z. Zhang, S. Yang, H. Li, Y. Zan, X. Li, Y. Zhu, M. Dou, F. Wang, Sustainable Carbonaceous Materials Derived from Biomass as Metal-Free Electrocatalysts, Adv. Mater. 31 (2019) 1805718. doi:10.1002/adma.201805718.
- 1423 [4] M. Inagaki, F. Kang, M. Toyoda, H. Konno, Carbon Materials for Adsorption of Molecules and Ions, Adv. Mater. 5 (2014) 335–361. doi:10.1016/b978-0-12-407789-8.00015-6.
- 1424 [5] M. R. Elamin, B. Y. Abdulkhair, A. O. Elzupir, Insight to aspirin sorption behavior on carbon nanotubes from aqueous solution: Thermodynamics, kinetics, influence of functionalization and solution parameters, Sci. Rep. 9 (2019) 12795. doi:10.1038/s41598-019-49331-6.
- 1425 [6] M. Ahmaruzzaman, D. Mohanta, A. Nath, Environmentally benign fabrication of SnO<sub>2</sub>-CNT nanohybrids and their multifunctional efficiency as an adsorbent, catalyst and antimicrobial agent for water decontamination, Sci. Rep. 9 (2019) 12795. doi:10.1038/s41598-019-49181-2.
- 1426 [7] S. T. Lim, J. H. Kim, C. Y. Lee, S. Koo, D. Jerng, S. Wongwises, H. S. Ahn, Mesoporous graphene adsorbents for the removal of toluene and xylene at various concentrations and its reusability, Sci. Rep. 9 (2019) 10922. doi:10.1038/s41598-019-47100-z.
- 1427 [8] M. Darvish Ganji, H. Kiyani, Molecular simulation of efficient removal of H<sub>2</sub>S pollutant by cyclodextrine functionalized CNTs, Sci. Rep. 9 (2019) 10605. doi:10.1038/s41598-019-46816-2.
- 1428 [9] A. A. Abia, E. D. Asuquo, Lead (II) and nickel (II) adsorption kinetics from aqueous metal solutions using chemically modified and unmodified agricultural adsorbents, Afr. J. Biotechnol. 5 (2006) 1475–1482.
- 1429 [10] R. Ahmad, S. Haseeb, Adsorption of Pb(II) on Mentha piperita carbon (MTC) in single and quaternary systems, Arab. J. Chem. 10 (2017) S412–S421. doi:10.1016/j.arabjc.2012.09.013.
- 1430 [11] A. Faccinetto, C. Focsa, P. Desgroux, M. Ziskind, Progress toward the Quantitative Analysis of PAHs Adsorbed on Soot by Laser Desorption/Laser Ionization/Time-of-Flight Mass Spectrometry, 1468

- 1469 Environ. Sci. Technol. 49 (2015) 10510–10520. 1534  
1470 doi:10.1021/acs.est.5b02703. 1535
- 1471 [12] O. B. Popovicheva, C. Irimiea, Y. Carpentier, I. K. 1536  
1472 Ortega, E. D. Kireeva, N. K. Shonija, J. Schwarz, 1537  
1473 M. Vojtišek-Lom, C. Focsa, Chemical composition 1538  
1474 of diesel/biodiesel particulate exhaust by FTIR spec- 1539  
1475 troscopy and mass spectrometry: Impact of fuel and 1540  
1476 driving cycle, *Aerosol Air Qual. Res.* 17 (2017) 1717– 1541  
1477 1734. doi:10.4209/aaqr.2017.04.0127. 1542
- 1478 [13] P. Parent, C. Laffon, I. Marhaba, D. Ferry, T. Z. Regier, 1543  
1479 I. K. Ortega, B. Chazallon, Y. Carpentier, C. Focsa, 1544  
1480 Nanoscale characterization of aircraft soot: A high- 1545  
1481 resolution transmission electron microscopy, Raman 1546  
1482 spectroscopy, X-ray photoelectron and near-edge X-ray 1547  
1483 absorption spectroscopy study, *Carbon* 101 (2016) 86– 1548  
1484 100. doi:10.1016/j.carbon.2016.01.040. 1549
- 1485 [14] D. L. Diggs, K. L. Harris, P. V. Rekhadevi, A. Ramesh, 1550  
1486 Tumor microsomal metabolism of the food toxicant, 1551  
1487 benzo(a)pyrene, in *Apc<sup>Min</sup>* mouse model of colon can- 1552  
1488 cer, *Tumor. Biol.* 33 (2012) 1255–1260. doi:10.1007/ 1553  
1489 s13277-012-0375-6. 1554
- 1490 [15] K. H. Kim, S. A. Jahan, E. Kabir, R. J. C. Brown, 1555  
1491 A review of airborne polycyclic aromatic hydrocarbons 1556  
1492 (PAHs) and their human health effects, *Environ. Int.* 1557  
1493 60 (2013) 71–80. doi:10.1016/j.envint.2013.07.019. 1558
- 1494 [16] G. Grimmer, *Environmental carcinogens: Polycyclic* 1559  
1495 *aromatic hydrocarbons: Chemistry, occurrence, bio-* 1560  
1496 *chemistry, carcinogenicity*, CRC Press, New York, 2018. 1561  
1497 doi:10.1201/9781351071758. 1562
- 1498 [17] C. A. Pope, D. W. Dockery, Health effects of fine 1563  
1499 particulate air pollution: Lines that connect, *J. Air* 1564  
1500 *Waste Manage. Assoc.* 56 (2006) 709–742. doi:10. 1565  
1501 1080/10473289.2006.10464485. 1566
- 1502 [18] B. A. Maher, I. A. Ahmed, V. Karloukovski, D. A. Ma- 1567  
1503 cLaren, P. G. Foulds, D. Allsop, D. M. Mann, R. Torres- 1568  
1504 Jardón, L. Calderon-Garciduenas, Magnetite pollution 1569  
1505 nanoparticles in the human brain, *Proc. Natl. Acad. Sci.* 1570  
1506 U.S.A. 113 (2016) 10797–10801. doi:10.1073/pnas. 1571  
1507 1605941113. 1572
- 1508 [19] N. D. Saenen, H. Bové, C. Steuwe, M. B. Roeffaers, 1573  
1509 E. B. Provost, W. Lefebvre, C. Vanpoucke, M. Ameloot, 1574  
1510 T. S. Nawrot, Children’s urinary environmental carbon 1575  
1511 load: A novel marker reflecting residential ambient air 1576  
1512 pollution exposure?, *Am. J. Respir. Crit. Care Med.* 196 1577  
1513 (2017) 873–881. doi:10.1164/rccm.201704-07970C. 1578
- 1514 [20] H. Bové, E. Bongaerts, E. Slenders, E. M. Bijmens, 1579  
1515 N. D. Saenen, W. Gyselaers, P. V. Eyken, M. Plusquin, 1580  
1516 M. B. J. Roeffaers, M. Ameloot, T. S. Nawrot, Am- 1581  
1517 bient black carbon particles reach the fetal side of hu- 1582  
1518 man placenta, *Nat. Commun.* 10 (2019) 3866. doi: 1583  
1519 10.1038/s41467-019-11654-3. 1584
- 1520 [21] A. A. Specht, M. W. Blades, Direct determination of 1585  
1521 polycyclic aromatic hydrocarbons in solid matrices us- 1586  
1522 ing laser desorption/laser photoionization ion trap mass 1587  
1523 spectrometry, *J. Am. Soc. Mass Spectrom.* 14 (2003) 1588  
1524 562–570. doi:10.1016/S1044-0305(03)00143-0. 1589
- 1525 [22] L. Basta, S. Veronesi, Y. Murata, Z. Dubois, N. Mishra, 1590  
1526 F. Fabbri, C. Coletti, S. Heun, A sensitive calorimetric 1591  
1527 technique to study energy (heat) exchange at the nano- 1592  
1528 scale, *Nanoscale* 10 (2018) 10079–10086. doi:10.1039/ 1593  
1529 C8NR00747K. 1594
- 1530 [23] C. T. Campbell, J. R. Sellers, Enthalpies and entropies 1595  
1531 of adsorption on well-defined oxide surfaces: Experi- 1596  
1532 mental measurements, *Chem. Rev.* 113 (2013) 4106– 1597  
1533 4135. doi:10.1021/cr300329s. 1598
- [24] A. Saha, A simultaneous volumetric adsorption– 1599  
isothermal titration calorimetry study of small 1600  
molecules on supported metallic nanoparticles, *J. 1601  
Therm. Anal. Calorim.* 124 (2016) 1623–1634. doi: 1602  
10.1007/s10973-016-5262-8. 1603
- [25] J. L. Falconer, J. A. Schwarz, Temperature- 1604  
programmed desorption and reaction: applications 1605  
to supported catalysts, *Cat. Rev.* 25 (1983) 141–227. 1606  
doi:10.1080/01614948308079666. 1607
- [26] R. A. Ketola, J. T. Kiuru, V. Tarkiainen, J. T. Kokko- 1608  
nen, J. Räsänen, T. Kotiaho, Detection of volatile 1609  
organic compounds by temperature-programmed des- 1610  
orption combined with mass spectrometry and fourier 1611  
transform infrared spectroscopy, *Anal. Chim. Acta.* 562 1612  
(2006) 245–251. doi:10.1016/j.aca.2006.01.069. 1613
- [27] J. T. Stuckless, D. E. Starr, D. J. Bald, C. T. Camp- 1614  
bell, J. T. Stuckless, D. E. Starr, D. J. Bald, C. T. 1615  
Campbell, Metal adsorption calorimetry and adhesion 1616  
energies on clean single-crystal surfaces Metal adsorp- 1617  
tion calorimetry and adhesion energies on clean single- 1618  
crystal surfaces, *J. Chem. Phys.* 107 (1997) 5547–5553. 1619  
doi:10.1063/1.474230. 1620
- [28] W. A. Brown, R. Kose, D. A. King, Femtomole Ad- 1621  
sorption Calorimetry on Single-Crystal Surfaces, *Chem.* 1622  
*Rev.* 98 (1998) 797–831. doi:10.1021/cr9700890. 1623
- [29] J. H. Fischer-Wolfarth, J. A. Farmer, J. M. Flores- 1624  
Camacho, A. Genest, I. V. Yudanov, N. Rösch, C. T. 1625  
Campbell, S. Schauermann, H.-J. Freund, Particle-size 1626  
dependent heats of adsorption of CO on supported 1627  
Pd nanoparticles as measured with a single-crystal mi- 1628  
crocalorimeter, *Phys. Rev. B* 81 (2010) 241416. doi: 1629  
10.1103/PhysRevB.81.241416. 1630
- [30] A. Faccinetto, P. Desgroux, M. Ziskind, E. Therssen, 1631  
C. Focsa, High-sensitivity detection of polycyclic aro- 1632  
matic hydrocarbons adsorbed onto soot particles us- 1633  
ing laser desorption/laser ionization/time-of-flight mass 1634  
spectrometry: An approach to studying the soot incep- 1635  
tion process in low-pressure flames, *Combust. Flame* 1636  
158 (2011) 227–239. doi:10.1016/j.combustflame. 1637  
2010.08.012. 1638
- [31] C. Miheșan, M. Ziskind, E. Therssen, P. Desgroux, 1639  
C. Focsa, IR laser resonant desorption of polycyclic aro- 1640  
matic hydrocarbons, *Chem. Phys. Lett.* 423 (2006) 407– 1641  
412. doi:10.1016/j.cplett.2006.04.032. 1642
- [32] C. Focsa, J. Destombes, Na/K (H<sub>2</sub>O) *n* clusters pro- 1643  
duced by laser desorption of Na/K salt doped ice, 1644  
*Chemical Physics Letters* 347 (2001) 390–396. doi: 1645  
10.1016/S0009-2614(01)01068-5. 1646
- [33] C. Miheșan, N. Lebrun, M. Ziskind, B. Chazallon, 1647  
C. Focsa, J. Destombes, Ir laser resonant desorption 1648  
of formaldehyde–H<sub>2</sub>O ices: hydrated cluster formation 1649  
and velocity distribution, *Surf. Sci.* 566 (2004) 650–658. 1650  
doi:10.1016/j.susc.2004.06.128. 1651
- [34] D. Delhayé, F. X. Ouf, D. Ferry, I. K. Ortega, O. Penan- 1652  
hoat, S. Peillon, F. Salm, X. Vancassel, C. Focsa, 1653  
C. Irimiea, N. Harivel, B. Perez, E. Quinton, J. Yon, 1654  
D. Gaffie, The MERMOSE project: Characterization 1655  
of particulate matter emissions of a commercial air- 1656  
craft engine, *J. Aerosol Sci.* 105 (2017) 48–63. doi: 1657  
10.1016/j.jaerosci.2016.11.018. 1658
- [35] L. D. Ngo, D. Duca, J. A. Noble, A. R. Ikhenazene, 1659  
M. Vojkovic, Y. Carpentier, C. Irimiea, Chemical dis- 1660  
crimination of the particulate and gas phases of mini- 1661  
CAST exhausts using a two-filter collection method, *At- 1662  
mospheric Measurement Techniques* 13 (2020) 951–967. 1663

- doi:10.5194/amt-13-951-2020. 1664
- [36] C. Mihean, M. Ziskind, E. Therssen, P. Desgroux, 1665  
C. Focsa, Parametric study of polycyclic aromatic hydro- 1666  
carbon laser desorption, *Journal of Physics: Condensed 1667*  
*Matter* 20 (2007) 025221. doi:10.1088/ 1668  
0953-8984/20/02/025221. 1669
- [37] A. Poretzky, D. Geohegan, G. Hurst, M. Buchanan, 1670  
B. Luk'yanchuk, Imaging of vapor plumes produced by 1671  
matrix assisted laser desorption: a plume sharpening 1672  
effect, *Phys. Rev. Lett.* 83 (1999) 444. doi:10.1103/ 1673  
*PhysRevLett.* 83.444. 1674
- [38] R. Zimmermann, M. Blumenstock, H. J. Heger, K. W. 1675  
Schramm, A. Kettrup, Emission of nonchlorinated and 1676  
chlorinated aromatics in the flue gas of incineration 1677  
plants during and after transient disturbances of combus- 1678  
tion conditions: Delayed emission effects, *Environ. Sci. Technol.* 35 (2001) 1019–1030. doi:10.1021/ 1680  
*es0001431.* 1681
- [39] E. Cappelli, C. Scilletta, S. Orlando, V. Valentini, 1682  
M. Servidori, Laser annealing of amorphous carbon 1683  
films, *Appl. Surf. Sci.* 255 (2009) 5620–5625. doi: 1684  
10.1016/j.apsusc.2008.10.062. 1685
- [40] J. P. Abrahamson, M. Singh, J. P. Mathews, R. L. Van- 1686  
der Wal, Pulsed laser annealing of carbon black, *Carbon* 1687  
124 (2017) 380–390. doi:10.1016/j.carbon.2017.08. 1688  
080. 1689
- [41] S. Ahn, D. Werner, H. K. Karapanagioti, D. R. Mc- 1690  
Glothlin, R. N. Zare, R. G. Luthy, Phenanthrene and 1691  
pyrene sorption and intraparticle diffusion in poly- 1692  
oxymethylene, coke, and activated carbon, *Environ. Sci. 1693*  
*Technol.* 39 (2005) 6516–6526. doi:10.1021/es050113o. 1694
- [42] R. Zacharia, H. Ulbricht, T. Hertel, Interlayer cohesive 1695  
energy of graphite from thermal desorption of polyaroma- 1696  
tic hydrocarbons, *Phys. Rev. B* 69 (2004) 155406. 1697  
doi:10.1103/PhysRevB.69.155406. 1698
- [43] R. J. Beuhler, E. Flanigan, L. J. Greene, L. Friedman, 1699  
Proton transfer mass spectrometry of peptides. rapid 1700  
heating technique for underivatized peptides containing 1701  
arginine, *J. Am. Chem. Soc.* 96 (1974) 3990–3999. doi: 1702  
10.1021/ja00819a043. 1703
- [44] L. P. Levine, J. F. Ready, E. Bernal, Gas desorption 1704  
produced by a giant pulse laser, *J. Appl. Phys.* 38 (1967) 1705  
331–336. doi:10.1063/1.1708977. 1706
- [45] K. Christmann, O. Schober, G. Ertl, M. Neumann, Ad- 1707  
sorption of hydrogen on nickel single crystal surfaces, 1708  
*The Journal of Chemical Physics* 4528 (1974) 4528– 1709  
4540. doi:10.1063/1.1680935. 1710
- [46] J. M. Chen, C. C. Chang, Laser desorption of submono- 1711  
layers of Na and Cs from Ge substrates, *J. Appl. Phys.* 1712  
43 (1972) 3884–3886. doi:10.1063/1.1661832. 1713
- [47] G. Wedler, H. Ruhmann, Laser induced thermal desor- 1714  
ption of carbon monoxide from Fe(110) surfaces, *Surf. 1715*  
*Sci.* 121 (1982) 464–486. doi:10.1016/0039-6028(82) 1716  
90255-2. 1717
- [48] H. Arnolds, C. Rehbein, G. Roberts, R. J. Levis, D. A. 1718  
King, Femtosecond Near-Infrared Laser Desorption of 1719  
Multilayer Benzene on Pt(111): A Molecular Newton's 1720  
Cradle?, *J. Phys. Chem. B* 104 (2002) 3375–3382. doi: 1721  
10.1021/jp993688e. 1722
- [49] J. L. Brand, S. M. George, Effects of laser pulse char- 1723  
acteristics and thermal desorption parameters on laser 1724  
induced thermal desorption, *Surf. Sci.* 167 (1986) 341– 1725  
362. doi:10.1016/0039-6028(86)90709-0. 1726
- [50] K. Dreisewerd, M. Schürenberg, M. Karas, F. Hil- 1727  
lenkamp, Influence of the laser intensity and spot size on 1728  
the desorption of molecules and ions in matrix-assisted  
laser desorption/ionization with a uniform beam profile,  
*Int. J. Mass Spectrom. Ion Process.* 141 (1995) 127–148.  
doi:10.1016/0168-1176(94)04108-J.
- [51] K. Oure, V. G. Lifshits, A. A. Saranin, A. V. Zo- 1729  
tov, M. Katayama, *Surface Science: An Introduction*, 1730  
Springer, Berlin, 2003.
- [52] R. M. Bouglas, *Principles of adsorption and adsorption 1731*  
processes, Wiley-Interscience publication, New York, 1732  
1984.
- [53] K. Christmann, *Introduction to Surface Physical Chem- 1733*  
istry, Springer, Heidelberg, 1991.
- [54] L. V. Zhigilei, B. J. Garrison, Molecular dynamics sim- 1734  
ulation study of the fluence dependence of particle yield 1735  
and plume composition in laser desorption and ablation 1736  
of organic solids, *Appl. Phys. Lett.* 74 (1999) 1341–1343.  
doi:10.1063/1.123544. 1737
- [55] S. Kuper, J. Brannon, K. Brannon, Threshold behavior 1738  
in polyimide photoablation: Single-shot rate measure- 1739  
ments and surface-temperature modeling, *Appl. Phys. 1740*  
*A* 56 (1993) 43–50. doi:10.1007/BF00351902. 1741
- [56] W. H. Dalzell, a. F. Sarofim, Optical Constants of Soot 1742  
and Their Application to Heat-Flux Calculations, *J. 1743*  
*Heat Transfer* 91 (1969) 100. doi:10.1115/1.3580063. 1744
- [57] A. B. Djurišić, E. H. Li, Optical properties of graphite, 1745  
*J. Appl. Phys.* 85 (1999) 7404–7410. doi:10.1063/1. 1746  
369370. 1747
- [58] R. J. M. Konings, *Comprehensive Nuclear Materials, 1748*  
Material Properties - Oxide Fuels for Light Water Reac- 1749  
tors and Fast Neutron Reactors, Elsevier, Amsterdam, 1750  
2012. doi:10.1016/B978-0-08-056033-5.90001-6. 1751
- [59] A. Butland, R. Maddison, The specific heat of graphite: 1752  
an evaluation of measurements, *J. Nucl. Mater.* 49 1753  
(1973) 45–56. doi:10.1016/0022-3115(73)90060-3. 1754
- [60] A. Guilloateau, M. L. Nguyen, Y. Bedjanian, G. Le Bras, 1755  
Desorption of polycyclic aromatic hydrocarbons from 1756  
soot surface: Pyrene and fluoranthene, *J. Phys. Chem. 1757*  
*A* 112 (2008) 10552–10559. doi:10.1021/jp803043s. 1758
- [61] Y. Bedjanian, M. L. Nguyen, A. Guilloateau, Desorption 1759  
of polycyclic aromatic hydrocarbons from soot surface: 1760  
Five- and six-ring (C<sub>22</sub>, C<sub>24</sub>) PAHS, *J. Phys. Chem. A* 1761  
114 (2010) 3533–3539. doi:10.1021/jp912110b. 1762
- [62] A. Bogaerts, Z. Chen, R. Gijbels, A. Vertes, Laser abla- 1763  
tion for analytical sampling: what can we learn from 1764  
modeling?, *Spectrochim. Acta B* 58 (2003) 1867–1893.  
doi:10.1016/j.sab.2003.08.004. 1765
- [63] D. Burgess Jr., P. C. Stair, E. Weitz, Calculations of the 1766  
surface temperature rise and desorption temperature in 1767  
laser-induced thermal desorption, *J. Vac. Sci. Technol.* 1768  
*A* 4 (1986) 1362 – 1366. doi:10.1116/1.573571. 1769
- [64] P. C. Stair, E. Weitz, Pulsed-laser-induced desorption 1770  
from metal surfaces, *J. Opt. Soc. Am. B* 4 (1987) 255– 1771  
260. doi:10.1364/JOSAB.4.000255. 1772
- [65] J. Ho, C. Grigoropoulos, J. Humphrey, Computational 1773  
study of heat transfer and gas dynamics in the pulsed 1774  
laser evaporation of metals, *J. Appl. Phys.* 78 (1995) 1775  
4696–4709. doi:10.1063/1.359817. 1776
- [66] J. Bechtel, Heating of solid targets with laser pulses, 1777  
*J. Appl. Phys.* 46 (1975) 1585–1593. doi:10.1063/1. 1778  
321760. 1779
- [67] E. V. Gurentsov, A review on determining the refractive 1780  
index function, thermal accommodation coefficient and 1781  
evaporation temperature of light-absorbing nanoparticles 1782  
suspended in the gas phase using the laser-induced 1783  
incandescence, *Nanotechnol. Rev.* 7 (2018) 583–604. 1784

- doi:10.1515/ntrev-2018-0080. 1794
- [68] J. P. Cummings, J. T. Walsh Jr, Erbium laser ablation: 1795  
the effect of dynamic optical properties, *Appl. Phys. Lett.* 62 (1993) 1988–1990. doi:10.1063/1.109512. 1797
- [69] W. D. Ciro, E. G. Eddings, A. F. Sarofim, Experimental 1798  
and numerical investigation of transient soot buildup 1799  
on a cylindrical container immersed in a jet fuel pool 1800  
fire, *Combust. Sci. Technol.* 178 (2006) 2199–2218. doi: 1801  
10.1080/00102200600626108. 1802
- [70] C. Pradère, J.-C. Batsale, J.-M. Goyhénèche, R. Pailler, 1803  
S. Dilhaire, Thermal properties of carbon fibers at very 1804  
high temperature, *Carbon* 47 (2009) 737–743. doi:10. 1805  
1016/j.carbon.2008.11.015. 1806
- [71] K. A. Fichthorn, R. A. Miron, Thermal desorption of 1807  
large molecules from solid surfaces, *Phys. Rev. Lett.* 89 1808  
(2002) 196103. doi:10.1103/PhysRevLett.89.196103. 1809
- [72] X. L. Han, Monte Carlo Least-Squares Fitting of Ex- 1810  
perimental Signal Waveforms Random Walk Method 1811  
Testing the Fitting Algorithm, *J. Comput. Sci.* 4 1812  
(2006) 1548–1555, URL: [https://digitalcommons. 1813](https://digitalcommons.butler.edu/facsch_papers/750)  
[butler.edu/facsch\\_papers/750](https://digitalcommons.butler.edu/facsch_papers/750). 1814
- [73] S. H. Lee, D. M. Murphy, D. S. Thomson, A. M. Mid- 1815  
dlebrook, Chemical components of single particles mea- 1816  
sured with particle analysis by laser mass spectrome- 1817  
try (PALMS) during the Atlanta supersite project: Fo- 1818  
cus on organic/sulfate, lead, soot, and mineral par- 1819  
ticles, *J. Geophys. Res.* 107 (2002) AAC1–13. doi: 1820  
10.1029/2000JD000011. 1821
- [74] Y. Zhang, X. Wang, H. Chen, X. Yang, J. Chen, 1822  
J. O. Allen, Source apportionment of lead-containing 1823  
aerosol particles in shanghai using single particle mass 1824  
spectrometry, *Chemosphere* 74 (2009) 501–507. doi: 1825  
10.1016/j.chemosphere.2008.10.004. 1826
- [75] M. Sekar, V. Sakthi, S. Rengaraj, Kinetics and equilib- 1827  
rium adsorption study of lead (II) onto activated car- 1828  
bon prepared from coconut shell, *J. Colloid Interface 1829*  
*Sci.* 279 (2004) 307–313. doi:10.1016/j.jcis.2004. 1830  
06.042. 1831
- [76] T. A. Saleh, Nanocomposite of carbon nanotubes/silica 1832  
nanoparticles and their use for adsorption of Pb(II): 1833  
from surface properties to sorption mechanism, *Des- 1834*  
*alination Water Treat.* 57 (2016) 10730–10744. doi: 1835  
10.1080/19443994.2015.1036784. 1836
- [77] E. Bottani, J. M. Tascon, Adsorption of Inorganic 1837  
Species from Aqueous Solutions. Adsorption by Car- 1838  
bon, Elsevier, Amsterdam, 2008. doi:10.1016/ 1839  
B978-0-08-056033-5.90001-6. 1840
- [78] J. P. Chen, X. Wang, Removing copper, zinc, and lead 1841  
ion by granular activated carbon in pretreated fixed- 1842  
bed columns, *Sep. Purif. Technol.* 19 (2000) 157–167. 1843  
doi:10.1016/S1383-5866(99)00069-6. 1844
- [79] K. Kadirvelu, C. Faur-Brasquet, P. L. Cloirec, Removal 1845  
of Cu(II), Pb(II), and Ni(II) by adsorption onto acti- 1846  
vated carbon cloths, *Langmuir* 16 (2000) 8404–8409. 1847  
doi:10.1021/1a0004810. 1848
- [80] Y. Zhang, C. Liu, W. Shi, Z. Wang, L. Dai, X. Zhang, 1849  
Direct measurements of the interaction between pyrene 1850  
and graphite in aqueous media by single molecule 1851  
force spectroscopy: Understanding the  $\pi$ - $\pi$  interac- 1852  
tions, *Langmuir* 23 (2007) 7911–7915. doi:10.1021/ 1853  
1a700876d. 1854
- [81] C. Ehli, N. Jux, D. Balbinot, G. M. A. Rah- 1855  
man, D. M. Guldi, F. Paolucci, M. Marcaccio, 1856  
D. Paolucci, M. Melle-Franco, F. Zerbetto, S. Campi- 1857  
delli, M. Prato, Interactions in Single Wall Carbon Nan- 1858  
otubes/Pyrene/Porphyrin Nanohybrids, *J. Am. Chem. 1859*  
*Soc.* 128 (2006) 11222–11231. doi:10.1021/ja0624974.
- [82] T. L. Sordo, J. A. Sordo, R. Flórez, Theoretical study 1860  
of adsorption of hydrocarbons on graphite, *J. Com- 1861*  
*put. Chem.* 11 (1990) 291–296. doi:10.1002/jcc. 1862  
540110303. 1863
- [83] J. T. Dickinson, J. J. Shin, S. C. Langford, The role 1864  
of defects in laser induced positive ion emission from 1865  
ionic crystals, *Appl. Surf. Sci.* 96-98 (1996) 316–320. 1866  
doi:10.1016/0169-4332(95)00436-X. 1867
- [84] D. Duca, C. Irimiea, A. Faccinnetto, J. A. Noble, M. Vo- 1868  
jkovic, Y. Carpentier, I. K. Ortega, C. Pirim, C. Focsa, 1869  
On the benefits of using multivariate analysis in mass 1870  
spectrometric studies of combustion-generated aerosols, 1871  
*Faraday Discuss.* 218 (2019) 115–137. doi:10.1039/ 1872  
C8FD00238J. 1873
- [85] C. Focsa, D. Duca, J. A. Noble, M. Vojkovic, Y. Car- 1874  
pentier, C. Pirim, C. Betrancourt, P. Desgroux, 1875  
T. Trischer, J. Spielvogel, M. Rahman, A. Boies, 1876  
K. F. Lee, A. N. Bhave, S. Legendre, O. Lancry, 1877  
P. Kreutziger, M. Rieker, Multi-technique physico- 1878  
chemical characterization of particles generated by a 1879  
gasoline engine: towards measuring tailpipe emissions 1880  
below 23 nm, *Atmos. Environ.* 235 (2020) 117642. doi: 1881  
10.1016/j.atmosenv.2020.117642. 1882
- [86] P. A. Turhanen, J. J. Vepsäläinen, S. Peräniemi, Ad- 1883  
vanced material and approach for metal ions removal 1884  
from aqueous solutions, *Sci. Rep.* 5 (2015) 8992. doi: 1885  
10.1038/srep08992. 1886
- [87] S. Cao, B. Li, R. Zhu, H. Pang, Design and synthe- 1887  
sis of covalent organic frameworks towards energy and 1888  
environment fields, *Chem. Eng. J.* 355 (2019) 602–623. 1889  
doi:10.1016/j.cej.2018.08.184. 1890
- [88] D. Benetti, R. Nouar, R. Nechache, H. Pepin, 1891  
A. Sarkissian, F. Rosei, J. MacLeod, Combined mag- 1892  
netron sputtering and pulsed laser deposition of  $TiO_2$  1893  
and  $BFCO$  thin films, *Sci. Rep.* 7 (2017) 2503–2512. 1894  
doi:10.1038/s41598-017-02284-0. 1895
- [89] H. Matsumura, H. Umemoto, K. K. Gleason, 1896  
R. Schropp, Catalytic Chemical Vapor Deposition: 1897  
Technology and Applications of Cat-CVD, Wiley-VCH, 1898  
Germany, 2019. 1899
- [90] J. Perrière, C. Hebert, N. Jedrecy, W. Seiler, O. Zanel- 1900  
lato, X. Portier, R. Perez-Casero, E. Millon, M. Nis- 1901  
tor, On the relevance of large scale pulsed-laser depo- 1902  
sition: Evidence of structural heterogeneities in ZnO 1903  
thin films, *J. Appl. Phys.* 116 (2014) 123502. doi: 1904  
10.1063/1.4896379. 1905
- [91] F. Chiarella, C. A. Perroni, F. Chianese, M. Barra, 1906  
G. M. De Luca, V. Cataudella, A. Cassinese, 1907  
Post-Deposition Wetting and Instabilities in Organic 1908  
Thin Films by Supersonic Molecular Beam Depo- 1909  
sition, *Sci. Rep.* 8 (2018) 12015. doi:10.1038/ 1910  
s41598-018-30567-7. 1911
- [92] C. Irimiea, A. Faccinnetto, X. Mercier, I. K. Ortega, 1912  
N. Nuns, E. Therssen, P. Desgroux, C. Focsa, Unveiling 1913  
trends in soot nucleation and growth: When secondary 1914  
ion mass spectrometry meets statistical analysis, *Car- 1915*  
*bon* 144 (2019) 815–830. doi:10.1016/j.carbon.2018. 1916  
12.015. 1917
- [93] C. Irimiea, A. Faccinnetto, Y. Carpentier, I. K. Ortega, 1918  
N. Nuns, E. Therssen, P. Desgroux, C. Focsa, A compre- 1919  
hensive protocol for chemical analysis of flame com- 1920  
bustion emissions by secondary ion mass spectrometry, 1921  
*Rapid Commun. Mass Spectrom.* 32 (2018) 1015–1025. 1922



1859 doi:10.1002/rcm.8133.  
1860 [94] J. Dunkley, M. Bucher, P. G. Ferreira, K. Moodley,  
1861 C. Skordis, Fast and reliable Markov chain Monte Carlo  
1862 technique for cosmological parameter estimation, *Mon.*  
1863 *Not. R. Astron. Soc.* 356 (2005) 925–936. doi:10.1111/  
1864 *j.1365-2966.2004.08464.x*.  
1865 [95] J. Akeret, S. Seehars, A. Amara, A. Refregier, A. Csil-  
1866 laghy, CosmoHammer: Cosmological parameter esti-  
1867 mation with the MCMC Hammer, *Astron. Comput.* 2  
1868 (2013) 27–39. doi:10.1016/j.ascom.2013.06.003.  
1869 [96] D. Foreman-Mackey, D. W. Hogg, D. Lang, J. Good-  
1870 man, EMCEE: The MCMC Hammer, *Publ. Astron.*  
1871 *Soc. Pac.* 125 (2012) 306–312. doi:10.1086/670067.  
1872 [97] S. T. Buckland, K. P. Burnham, N. H. Augustin, Model  
1873 selection: an integral part of inference, *Biometrics* 53  
1874 (1997) 603–618. doi:10.2307/2533961.  
1875 [98] D. R. Anderson, “Chapter 5: Multimodel inference” in  
1876 *Model based inference in the life sciences: A primer on*  
1877 *evidence*, Springer Science & Business Media LLC, New  
1878 York, 2007.